2013

Development of high-lift laminar wing using steady active flow control

Patrick Clayton
Iowa State University

Development of high-lift laminar wing using steady active flow control

by

Patrick J. Clayton

A thesis submitted to the graduate faculty

in partial fulfillment of the requirements for the degree of

MASTER OF SCIENCE

Major: Aerospace Engineering

Program of Study Committee:
Richard Wlezien, Major Professor
Hui Hu
Alric Rothmeyer
Thomas Ward

Iowa State University

Ames, Iowa

2013

TABLE OF CONTENTS

LIST OF FIGURES

LIST OF TABLES

ACKNOWLEDGMENTS

During my graduate studies at Iowa State University, I have had the pleasure of being surrounded by so many people who have motivated and supported me. I am grateful these people have helped me achieve the goals I set for myself. First, I want to thank my major professor, Dr. Richard Wlezien, for his patience, guidance, and advice throughout this research. Dr. Wlezien has pushed me and demanded a level of excellence in my work that I had not known previously. I am truly grateful for his belief in me.

Thank you, Bill Rickard, for your advice throughout the design and construction of the model. I also would like to extend my gratitude to all the undergraduate students in the WiST lab who were instrumental during the building and assembly of the entire test section and model, especially Anil Jairam.

I especially thankful to my fellow graduate students and friends, Lucas Clemons and Hephzibah Clemons. Lucas has been instrumental in the design of the airfoil, and his help made this project possible. Lucas and Hephzibah, your help, knowledge, and support have kept me going throughout this time.

Finally, I would like to thank all my friends and family who have supported me throughout my education. I am especially grateful to my parents, who have always believed in me and my ability to achieve the goals I set. I love you.

NOMENCLATURE

α – angle of attack

c – airfoil chord

$C_D = \frac{F_D}{q_\infty S}$ – Coefficient of Drag

$C_L = \frac{F_L}{q_\infty S}$ – Coefficient of Lift

$C_p = \frac{p - p_\infty}{q_\infty}$ – Coefficient of Pressure

$C_\mu = \frac{\rho_j U_j^2 h}{q_\infty c}$ – Coefficient of Momentum

$C_{\mu,1}$ = C_μ for forward-slot blowing at d/c = 0.01

$C_{\mu,2}$ = C_μ for mid-slot blowing at d/c = 0.10

$C_{\mu,3}$ = C_μ for aft-slot blowing at d/c = 0.80

F_D – Drag force – force parallel to freestream flow

F_L – Lift force – force perpendicular to freestream flow

h – slot height

ρ – density of fluid

$q_\infty = \frac{1}{2}\rho_\infty V_\infty^2$ – freestream dynamic pressure

d – slot chordwise location

S – airfoil planform area

$Re = \frac{\rho U c}{\mu}$ – chord Reynolds Number

U – flow velocity

Abbreviations

AFC – active flow control

AoA – angle of attack

BL – boundary layer

PFC – passive flow control

psf – pounds per square foot (lbs/ft^2)

RP – rapid-prototype

TO/L – take-off and landing

VG – vortex generator

Subscripts

∞ – freestream

j – jet

ABSTRACT

Fuel costs represent a large fraction of aircraft operating costs. Increased aircraft fuel efficiency is thus desirable. Laminar airfoils have the advantage of reduced cruise drag and increased fuel efficiency. Unfortunately, they cannot perform adequately during high-lift situations (i.e. takeoff and landing) due to low stall angles and low maximum lift caused by flow separation. Active flow control has shown the ability to prevent or mitigate separation effects, and increase maximum lift. This fact makes AFC technology a fitting solution for improving high-lift systems and reducing the need for slats and flap elements.

This study focused on experimentally investigating the effects of steady active flow control from three slots, located at 1%, 10%, and 80% chord, respectively, over a laminar airfoil with 45 degree deflected flap. A 30-inch-span airfoil model was designed, fabricated, and then tested in the Bill James 2.5'x3' Wind Tunnel at Iowa State University. Pressure data were collected along the mid-span of the airfoil, and lift and drag were calculated.

Five test cases with varying injection locations and varying C_μ were chosen: baseline, blown flap, leading edge blowing, equal blowing, and unequal blowing. Of these cases, unequal blowing achieved the greatest lift enhancement over the baseline. All cases were able to increase lift; however, gains were less than anticipated.

CHAPTER 1. INTRODUCTION

In past decades the growing global economy has come to rely upon inexpensive air travel for both commercial and private industry. The largest operating cost for modern aircrafts is fuel. According to the Federal Aviation Administration (FAA), a 1% reduction in fuel consumption could save 1.25 million dollars daily (Collis, Joslin, Seifert, & Theofilis, 2004). The dramatic increase in demand for air travel worldwide combined with the air travel industry's high exposure to increasing jet fuel prices has called for a step increase in efficiency of current air travel systems and immediate advancements to improve aircraft fuel efficiency. These factors—increased air travel and increased cost of jet fuel—have motivated companies to pursue technologies aimed at reducing fuel consumption.

During takeoff and landing (TO/L) airplanes generate increased lift and drag to reduce ground speed and runway lengths. Currently, modern aircraft use airfoils that are turbulent in cruise with high-lift elements, such as slats and flaps, to produce the lift necessary for TO/L. TO/L is the shortest portion of any flight; aircraft spend the majority of flight in cruise where lift requirements are lower. During cruise, turbulent flow produces higher skin friction drag which can represent over 50% of the total drag. By reducing drag, aircraft improve fuel efficiency. The use of laminar airfoils would significantly reduce skin friction drag and improve overall aircraft fuel efficiency. The benefits laminar airfoils have during cruise are significant, but their tendency to stall at low angles of attack (AoA) and low maximum lift make them impractical for TO/L situations. To address this problem, this research study was conducted to develop high-lift technology for laminar airfoils by using active flow control.

Flow Control

Flow control can be described as altering an airfoil's natural flow state and development to a more desirable state (Collis, 2004). Flow control has a long history, beginning with Prandtl's discovery of the boundary-layer (BL) in 1904 (as cited by Gad-El-Hak, 1991). Since this discovery, flow control has advanced from a purely empirical approach to a much higher understanding of the flow physics involved and has led to advancements in passive and active flow control.

Passive Flow Control

To date, passive flow control (PFC) remains the most utilized form of flow control, and has many varieties such as slats, flaps, vortex generators, riblets and strakes to name a few. These systems are used to control separation and increase lift during TO/L. Passive systems do not require power input and have the advantage of being easily implemented and maintained.

Leading edge slats, and trailing edge flaps exemplify the most utilized high-lift configurations and are forms of PFC. Both slats and flaps work under the same principle, where flow is accelerated from the high pressure side of an airfoil and injected over the suction side of the airfoil. This additional flow energizes the BL, enabling it to overcome more adverse pressure gradients, and remain attached at higher AoA. Without these PFC systems, separation occurs at high angles of attack and leads to stall. By remaining attached and preventing BL separation, higher stall angles can be achieved, the airfoil can continue to generate higher lift, and perform at lower speeds necessary for TO/L (Figure 1).

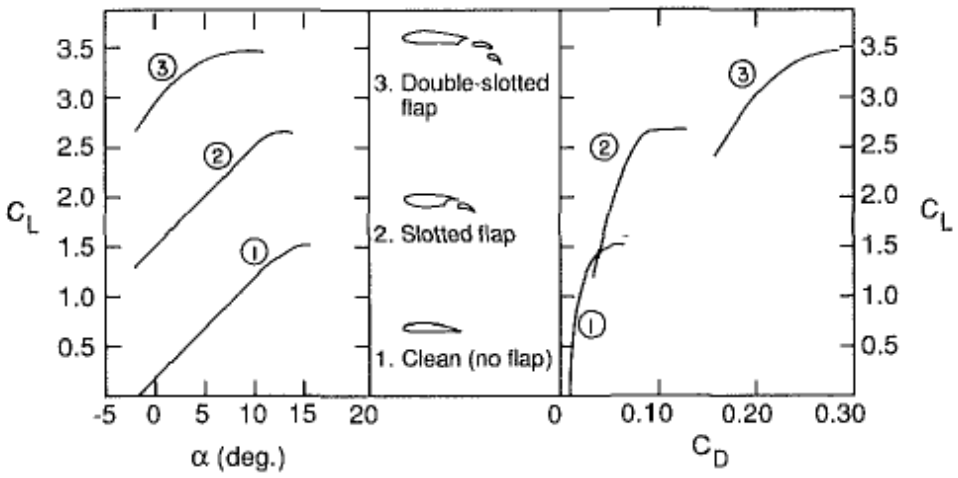

Figure 1. Passive flow control lift and drag effects (Gad-El-Hak, 1991)

Unfortunately, PFC systems come with high drag penalties during cruise due to their mechanical nature and introduction of discontinuities to the airfoil profile.

A secondary form of PFC, vortex generators (VG), are small high aspect-ratio airfoils mounted normally to lifting surfaces and ahead of the flow separation point (Figure 2). While flaps and slats use the injection of momentum into the boundary-layer to delay stall, vortex generators use the concept of vortex mixing to delay stall. VG's can be installed on various aircraft elements, including the airframe, engine nacelle and the wing. Once installed on an aircraft, VG's create tip vortices during flight which begin to entrain and mix the turbulent free-stream within the retarded BL. The addition of high speed free-stream flow reenergizes the BL, helping it overcome more adverse pressure gradients at higher angles of attack and prevent separation. However, typical VG's cannot be retracted while outside of their operation range, and begin to introduce additional profile drag penalties during cruise, which in turn decreases cruise system performance and fuel efficiency.

Figure 2. Vortex generators on a Dragonfly wing

Passive flow control technologies are highly effective over their short operating time, but their effects cannot entirely be removed outside of TO/L and become detrimental to aircraft efficiency during cruise. Replacing passive control systems (i.e. flaps and slats), would lead to reductions in mechanical complexity, gross takeoff weight, operating empty weight, and improvements in fuel efficiency (Schatz, 2004).

Active Flow Control

Active Flow Control (AFC) is not a new concept. After initially presenting the concept of two-dimensional separation in 1904 and effectively introducing Boundary-Layer Theory, Prandtl began experimenting with the effects of flow control via suction to improve flow attachment to a solid body. Since then, flow control has been further studied as a method of separation control, with benefits such as enhanced lift, reduced drag and noise emissions, and improved fuel efficiency. As previously stated, Passive Flow Control (PFC) systems such as flaps and vortex generators represent the majority of flow control systems but, due to their size and complexity, they can increase the overall weight and profile drag

during cruise which, in turn, decreases the fuel efficiency of any aircraft. AFC has the capability to solve these issues and reduce the need for PFC systems. AFC systems use direct addition of momentum into the BL, typically from a slot or row of small orifices, to achieve the same results as PFC without introducing steps, gaps and other discontinuities which cause aircraft inefficiency.

AFC has been demonstrated in many different forms and has been researched for uses in various fields. AFC is commonly used for separation control achieved through steady blowing, periodic (or pulsed) excitation, or acoustic excitation. Both steady blowing and periodic excitation consist of directly inject momentum into the BL by blowing air through a slot. Acoustic excitation focuses on stimulating BL flow instabilities with sound to increase near wall momentum. This section will concentrate primarily on steady blowing as it was the focus of this project.

Steady blowing has been to shown to be most effective when momentum is added near the leading-edge of an airfoil (i.e. $x/c \leq 10\%$), or before the shoulder of a deflected flap. Blowing over a deflected flap, also referred to as Coanda blowing, prevents separation effects are prevented by utilizing the Coanda effect, which is defined as the tendency of jet to stay attached to adjacent curved wall (Nichino, 2010). Figure 3 demonstrates the effects of coanda blowing. When using a Coanda flap the complexity of the system can be reduced with respect to a traditional fowler flap because the flap can rotate around a simple hinge, without creating unnecessary gaps.

Finally, it must to be noted that, the effects of steady blowing have been well documented. It has been shown that periodic excitation can achieve similar results as steady

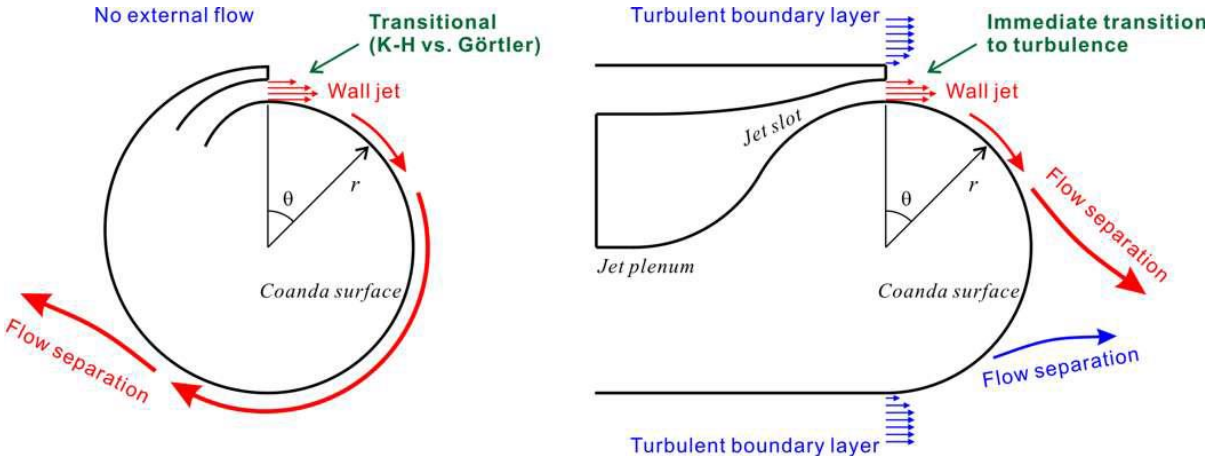

Figure 3. Coanda effect (a) over a cylinder (b) over airfoil rounded trailing edge (Nichino, 2010)

blowing with much less momentum addition, but the current study focused exclusively on the effects of steady blowing as a basis for further future periodic excitation investigations.

Non-dimensional Parameters

Non-dimensional parameters affect the performance of the airfoil; therefore, it is important to define the terms that are used to judge the performance of the airfoil. The first parameters of interest are the coefficient of lift (C_L) and the coefficient of drag (C_D). By definition, lift and drag are the components of aerodynamic force perpendicular to the incoming freestream velocity. Coefficient of lift and drag are dimensionless ratios between lift and drag force to the freestream dynamic pressure (q_∞), respectively (Anderson, 2011). These terms are represented as:

$$q_\infty = \frac{1}{2}\rho_\infty U_\infty^2 \tag{1}$$

$$C_L = \frac{F_L}{q_\infty S} \tag{2}$$

$$C_D = \frac{F_D}{q_\infty S} \tag{3}$$

where F_L and F_D are lift and drag force, respectively, and the variables ρ_∞, V_∞, and S represent the freestream density, velocity, and the airfoil planform area, respectively.

In this study, C_L and C_D were calculated using the pressure distribution around the airfoil. These pressures are shown using the dimensionless pressure coefficient (C_p) defined as follows:

$$C_p = \frac{p - p_\infty}{q_\infty} \tag{4}$$

In this equation, p_∞ is the upstream static pressure and p is the pressure at a given location.

Finally, in addition to the coefficients that describe aerodynamic forces, it is necessary to define a term that describes the addition of momentum used in active flow control. Aptly called the momentum coefficient (C_μ), this term was first used when Poisson-Quinton (as cited by Greenblatt, 2000) discovered that separation control is governed by momentum (rather than mass) addition. Momentum coefficient is defined as

$$C_\mu = \frac{\rho_j U_j^2 h}{q_\infty c} \tag{5}$$

where h and c are slot height and chord length, and the variables ρ_j and U_j are jet conditions of density and velocity, respectively. C_μ is a ratio of jet momentum to freestream momentum. This term helps quantify the amount of energy that is added to the system. By controlling separation via momentum addition, the effects on C_L and C_D can dramatic. However, for the system to be efficient, the gained system performance must exceed the required energy expenditure.

Objectives

The objectives of this research were broken down into three major categories and are listed as follows:

1. Successfully designing and fabricating an AFC high-lift laminar wing which is scaled down from the 8 ft. model profile provided by Northrop Grumman. Along with this is the design and assembly of a test section which would enable the wing to be tested in the ISU Bill James wind tunnel.
2. Determining if C_L can be substantially increased through the use of steady active flow control at varying C_μ levels.
3. Determining the effects of multiple slot blowing from the forward, mid, and aft slots on C_L & C_D.

CHAPTER 2. LITERATURE REVIEW

Numerous researchers have looked into AFC technologies for the purposes of enhancing lift and delaying stall. The studies presented in the following section have investigated the effects of steady blowing at the leading edge and before a deflected flap. Only one of these studies has investigated the effects of steady blowing at both of these locations simultaneously.

Previous Studies

In previous experimental studies by Seifert (1996) and Bright (2012), and numerical studies by Pfingsten (2005) and Burnazzi (2012), the researchers have investigated steady blowing and its ability to enhance lift in high-lift configurations (i.e. deflected flap). Each of these works are important to the present study because they characterize the effects of steady blowing at different chord locations, and show that steady AFC can successfully reenergize the BL, improve separation, and increase $C_{L,max}$. The present study looked to relate its results to these findings.

The experimental work by Seifert (1996) investigated the effects of steady and oscillatory blowing on four different airfoils (Figure 4). Of these four airfoils, a NACA 0015 airfoil was used to study steady LE blowing as well as steady blowing from a 20° deflected flap. This work showed that in both steady and oscillatory cases blowing over a deflected flap is much more effective in increasing $C_{L,max}$ than LE blowing alone at the same C_{μ}. Only strong LE blowing, which required approximately four times the C_{μ} of deflected flap

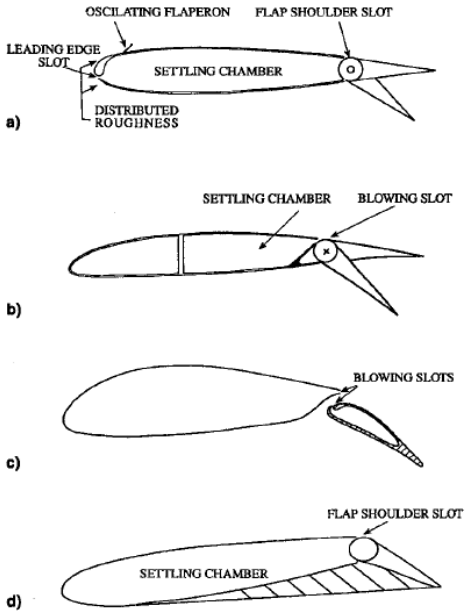

Fig. 1 Sketch of the airfoils tested: a) NACA 0015, b) E214F, c) PR8-40, and d) SPCA-1.

Figure 4. Sketch of the airfoils tested by Seifert (1996)

blowing, was able to obtain similar results as shoulder flap blowing. This study also showed that steady LE blowing had little to no effect on C_L before $C_\mu \geq 1.5\%$, even being somewhat detrimental before this point, and not seeing steady gains until $C_\mu \geq 3\%$. Figure 5 shows the results from Seifert's test for steady blowing and oscillatory blowing. Here $<c\mu>$ represents the oscillatory blowing momentum coefficient. This is consistent with other AFC studies. In the three other experiments from this study, blowing is applied exclusively at the flap. Each of these experiments show that steady blowing is effective in preventing separation and increasing $C_{L,max}$.

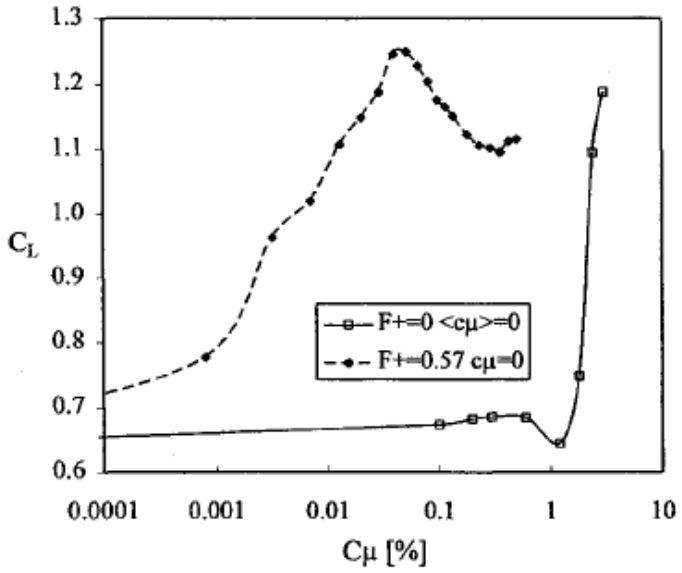

Figure 5. Effects of cμ and <cμ> on C_L of the NACA 0015 (Seifert, 1996)

Pfingsten (2005) and Burnazzi (2012), used CFD to numerically demonstrate the effects of steady blowing directly upstream from a deflected flap. Pfingsten focuses on the variation of slot height and size of deflected flap. The circulation control simulations have slot heights, flap size and flap deflection (η) similar to the present study. In the simulation most directly comparable to the current study (h/c = 0.001, η=40°, C_μ=.03), Pfingsten's findings predict an almost 100% increase in maximum lift over the baseline, with $C_{L,\,max}\approx 4$ coming at α = 5°. Similar to Pfingsten, Burnazzi looks into the effects of blowing upstream of a deflected flap but with the addition of a drooped-nose. The "clean nose" configuration has a 65° deflected flap. Simulations were then run on the clean nose and the drooped-nose at varying size and angle of deflection. For the clean nose configuration, the achievable $C_{L,max}$ is shown to be fairly high even at lower C_μ values, but the stall angle is low and continues to drop with increased blowing (Figure 6).

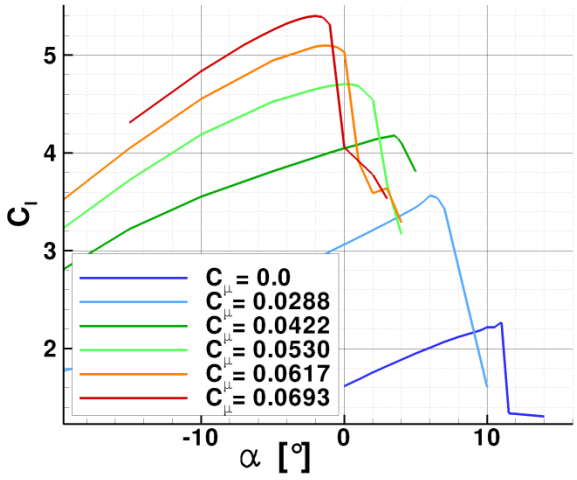

Figure 6. Lift vs. AoA for steady blowing over a deflected flap (Burnazzi, 2012)

Finally, the experimental research by Bright (2012) is a continuation of the work previously mentioned. Since the effects of TE deflected flap blowing are well documented, this study focuses on the addition of steady AFC around the LE to create high-lift. Bright (2012) uses steady LE blowing in conjunction with blowing over a 45° deflected flap on both "clean nose" and deflected nose configurations. For the clean nose configuration, two LE slots are used with a third directly before the flap. The profile for the clean nose configuration is shown in Figure 7.

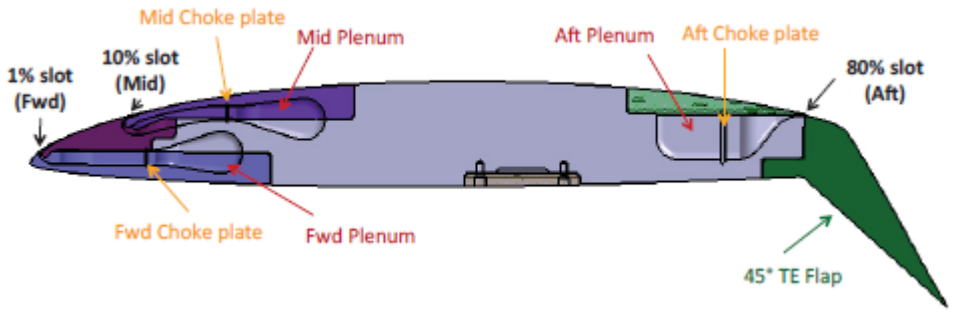

Figure 7. Airfoil profile with slot location and plenum detail (Bright, 2012)

Bright (2012) confirmed experimentally the effects of the TE deflected flap blowing before testing the effectiveness of additional LE blowing. Bright tested the effectiveness of the 1% slot, along with the effectiveness of the 1% and 10% slot together with varying C_μ. The most successful test utilizes differential blowing. In this test, the 10% slot C_μ is varied while the 1% and 10% slot are kept constant. The results from this test are shown in Figure 8.

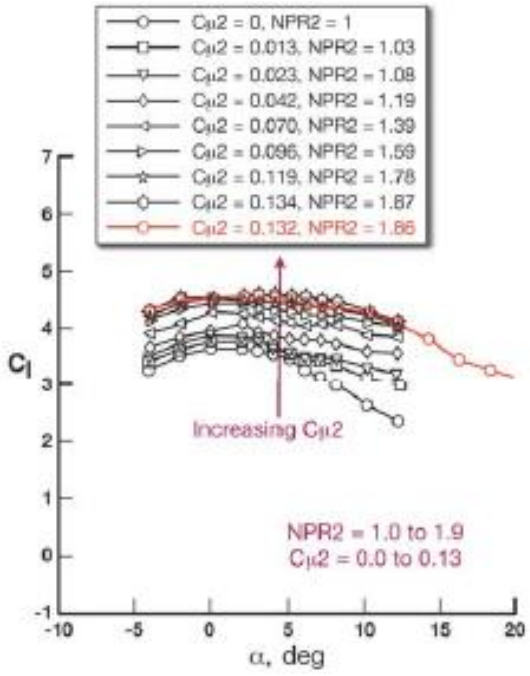

Figure 8. Effect of differential LE slot blowing with varying LE blowing at 10% chord (Cμ2); Cμ1 = 0.056 and Cμ3 = 0.035. (Bright, 2012)

As shown in Figure 8, differential blowing is able to achieve a maximum lift of 4.6 along with gradual stall characteristics. The additional momentum from both LE slots helps delay the effects of stall past 10°, and prevent the sharp drop off in lift as Burnazzi's work predicted. Instead, the stall effects are mild, and the airfoil is able to generate C_L values greater than 4 till $\alpha \approx 12°$. Finally, Figure 9 shows pressure distributions from Bright (2012)

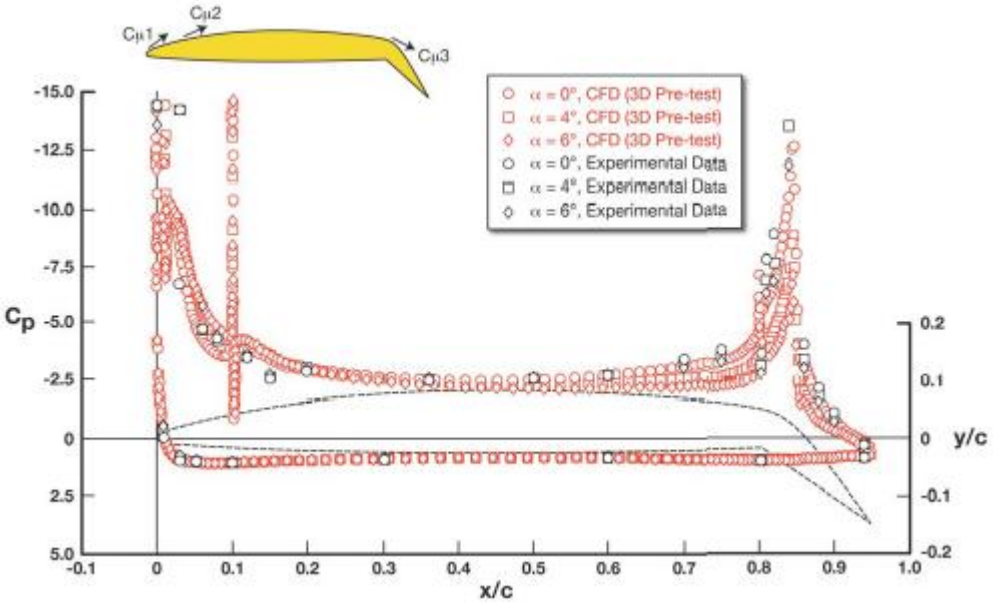

Figure 9. Comparison of pressure distributions of CFD and experimental results; Cμ1 = 0.12, Cμ2 = 0.13, and Cμ3 = 0.04. (Bright, 2012)

for both the CFD and experimental results. The pressure distributions in Figure 9 further confirm that the forward slots were successful in creating high-lift around the LE of the airfoil and the shoulder of the deflected flap. The goal of the current research study is to achieve similar results as Bright (2012).

CHAPTER 3. DESIGN AND METHODOLOGY

Wind Tunnel

The Iowa State University Bill James wind tunnel, located in the Wind Simulation and Testing Laboratory (WiST Lab), was used in these experiments. It has an 8ft long test section with a rectangular 3ft by 2.5ft cross section. The open circuit tunnel design utilizes a large contraction section located upstream of the test section and a large fan located downstream of the test section to generate air speeds up to 180 mph (Figure 10).

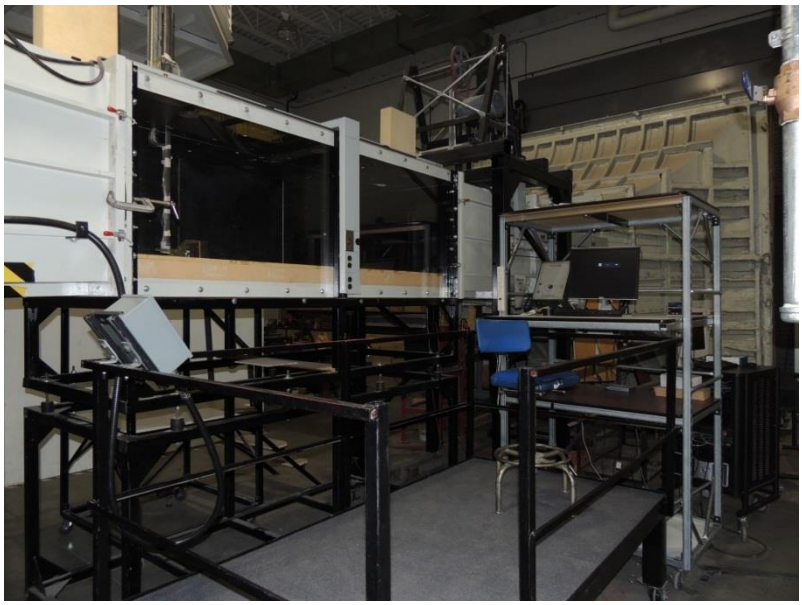

Figure 10. Bill James Wind Tunnel (8 ft. test section and upstream contraction shown)

The fan is powered by a 100 hp, 3-phase, 440-volt motor. The electronic control box is capable of adjusting motor frequency in increments of 0.1 Hz. Changing motor frequency gave the ability to control tunnel wind speed, maintain dynamic pressure (q_∞), and generate the proper C_μ values during testing. Figure 11 shows the wind speed of the wind tunnel

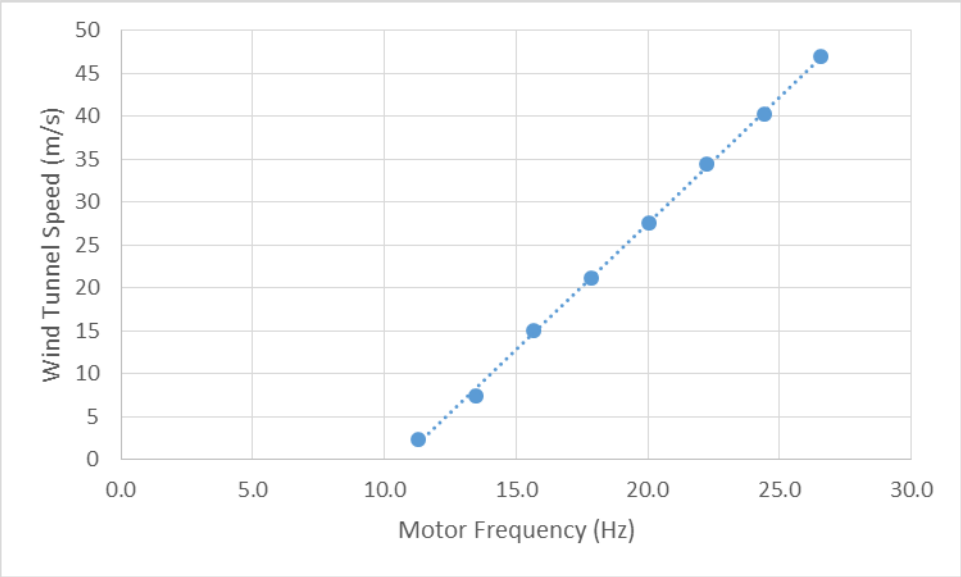

Figure 11. Bill James wind tunnel speed v. motor frequency (wind tunnel empty)

while empty v. motor frequency. Freestream velocities were determined by using the wind tunnel's pitot probe connected to a DTC Series ESP Scanner. A second scanner was used inside the airfoil for acquiring pressure distribution data. Details for these scanners are given the Pressure Measurement System section.

Test Section

The 8 ft. test section of the Bill James wind tunnel is broken into two smaller 4 ft. sections for this study. Upstream, in the first 4 ft. of the testing section a previously constructed test section is installed. This test section is used solely as a place holder, and no instrumentation is installed in this section. Downstream, a second 4 ft. test section is installed which is designed specifically for supporting the model, rotating through AoA sweeps, and supporting the air supply system (RP adapters, PVC couplings, and PVC hoses) which feeds air to the airfoil plenums. Shown in Figure 12 are a basic SolidWorks drawing

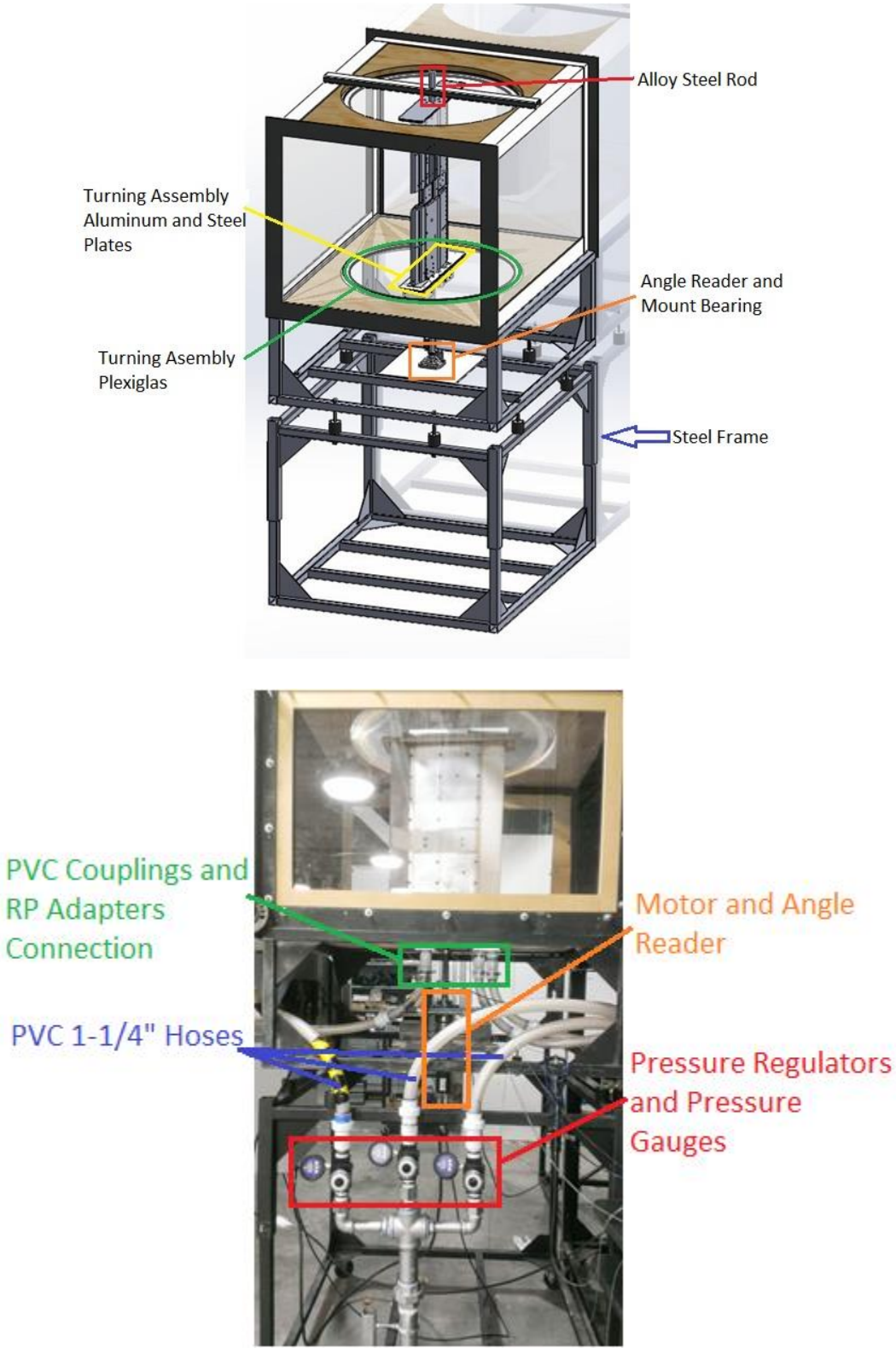

Figure 12. Test Section (a) SolidWorks drawing, and (b) air supply system with details

of this test section without the motor and the final test section assembly with details on the air supply system.

This test section can be broken down into four major components:

1. The supporting steel frame and alloy steel rod;
2. The turning assembly which includes the aluminum and steel plates with connecting Plexiglas panels;
3. The motor and angle reader;
4. The air supply system including the RP adapters, PVC couplings, and PVC hoses.

The testing area is supported by the steel frame assembly underneath. These two box frames can be height adjusted in order to be properly aligned with the Bill James wind tunnel. Eight vibration isolators also enable the test section to be properly leveled prior to testing (Figure 12). A 1 inch alloy steel rod, which runs vertically through the test section, is supported by this steel frame via an attached ball bearing mount which also enables it to rotate freely. The entire airfoil assembly, including the aluminum and steel plates, the motor and angle reader, and the air supply system, are then supported off this 1 inch alloy steel rod.

Plexiglas panels are installed on all four inner walls of the test section. This gives clear view inside the wind tunnel and a smooth boundary surface. The airfoil is installed vertically in the wind tunnel and spans the full height of the test section. The weight of the airfoil assembly is too much for it to be supported by the Plexiglas alone, and the air supply hoses have to rotate with the airfoil while not imparting any additional loads. To solve these issues, a turning assembly has been designed that attaches at the top and bottom of the airfoil, is able to rotate in unison with the airfoil, and supports both the airfoil and air supply

systems. First, two 30 inch circular Plexiglas "cut-outs" were fabricated. These cut-outs complete the inside walls of the test section, and the edges have stepped design which is lined with 3M™ PTFE tape that helps seal the tunnel during testing and reduce friction as the system rotates. Rectangular aluminum plates have been attached on either side of the airfoil and embedded in the Plexiglas cut outs (Figure 13). These plates are then bolted together with the Plexiglas so that the assembly turns in unison.

Figure 13. Airfoil assembly in test section with attached turning system

Aluminum can be easily machined and is less prone to corrosion which makes it a good mating surface for the airfoil assembly; however, it is also flexible and deflects under the weight of the model which could cause air leakage problems once the airfoil plenums are pressurized. To prevent the aluminum from deflecting, each aluminum plate is reinforced

with steel on the outside of the test section (Figure 14). Steel is strong enough to prevent the aluminum plate from deflecting under the weight of the airfoil, and also allowed for compression plates to be installed above each plenum to further compress the plenums and prevent air leakage. This entire turning system is placed at the top and bottom of the test section enabling the model to freely rotate through AoA sweeps (Figure 13). During testing, AoA was changed between 0 and 10 degrees.

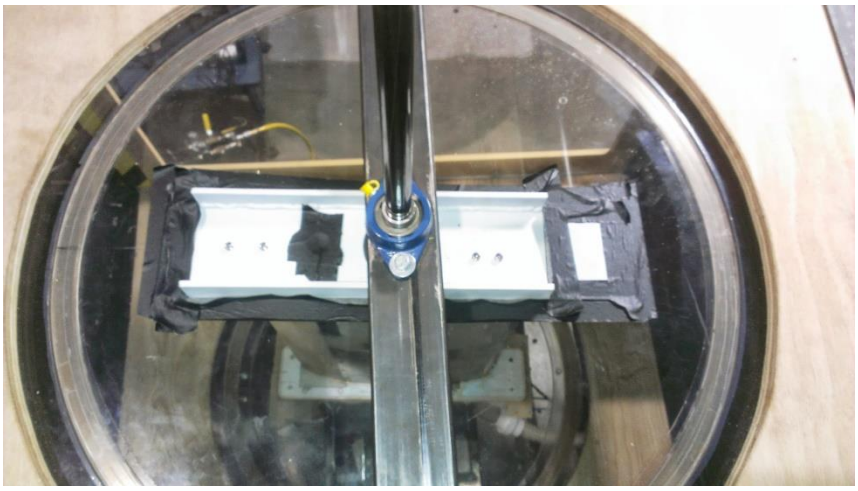

Figure 14. Steel reinforcing plate

To rotate the entire airfoil and turning assembly, the bottom of the 1 inch alloy steel rod is coupled to a Kollmorgen AKM23C Brushless Servomotor with 100:1 gearbox ratio (Figure 15). This motor is capable of producing 800 lb-in of torque, enough to keep the airfoil in position during AoA sweeps. In conjunction with the Kollmorgen AKD Servo Drive and Workbench software, the motor position could be changed with three decimal places of accuracy; however, a combination of factors including the size of the system and the high amount of torque generated during testing make this level of accuracy impossible to maintain during testing. For these reasons, one decimal of accuracy for angle readings was

Figure 15. Kollmorgen AKM23C Servomotor with 100:1 gearbox

assumed during testing. Zero AoA was set at the beginning of testing based on the non-deflected airfoil profile and marked for reference. From this point on AoA was controlled using the Workbench software. For a visual read out and confirmation of angle an ASM PMIR7 Magnetic Code Wheel, PMIS4 Sensor Head, and PRODIS Digital Process Meter were used together. During testing the small angle fluctuations of the system, between 0.1-0.4 degrees, were confirmed by the ASM angle sensor. Both digital process meter and the magnetic code wheel and sensor head are shown in Figure 16.

Airfoil design

Northrop Grumman Corporation provided the baseline high-lift airfoil profile used in this study, which in a non-deflected configuration is able to achieve laminar cruise conditions. This section covers the design of this airfoil assembly along with details on the air supply systems.

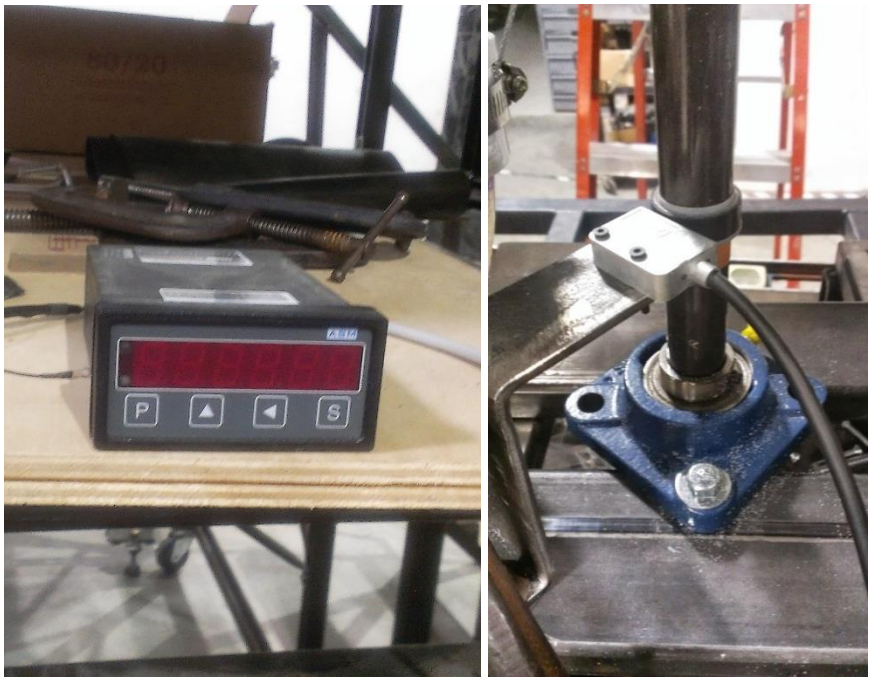

Figure 16. (a) PRODIS Digital Process meter, and (b) ASM Sensor head and magnetic code wheel

The airfoil has a unique geometry, with a sharp leading edge and maximum thickness at approximately mid chord. This study utilized a high lift configuration airfoil with a constant 45 degree deflected trailing edge. The model has an overall span of 30 inches and a deflected chord of 18 inches. Figure 17 shows a drawing of the airfoil profile and full assembly.

The airfoil assembly is broken into 4 major sections: the leading edge RP assembly, the aft RP assembly, the aluminum core, and the aluminum deflected tail with RP pressure port section. The leading edge and aft sections, house the 1% and 10% slot pressurized plenums, and the 80% slot pressurized plenum, respectively. The leading edge, aft, and deflected trailing edge with pressure taps sections are all built up from VeroWhite plastic, a rapid prototyping material, by using an Objet260 Connex 3D printer from Stratasys. By

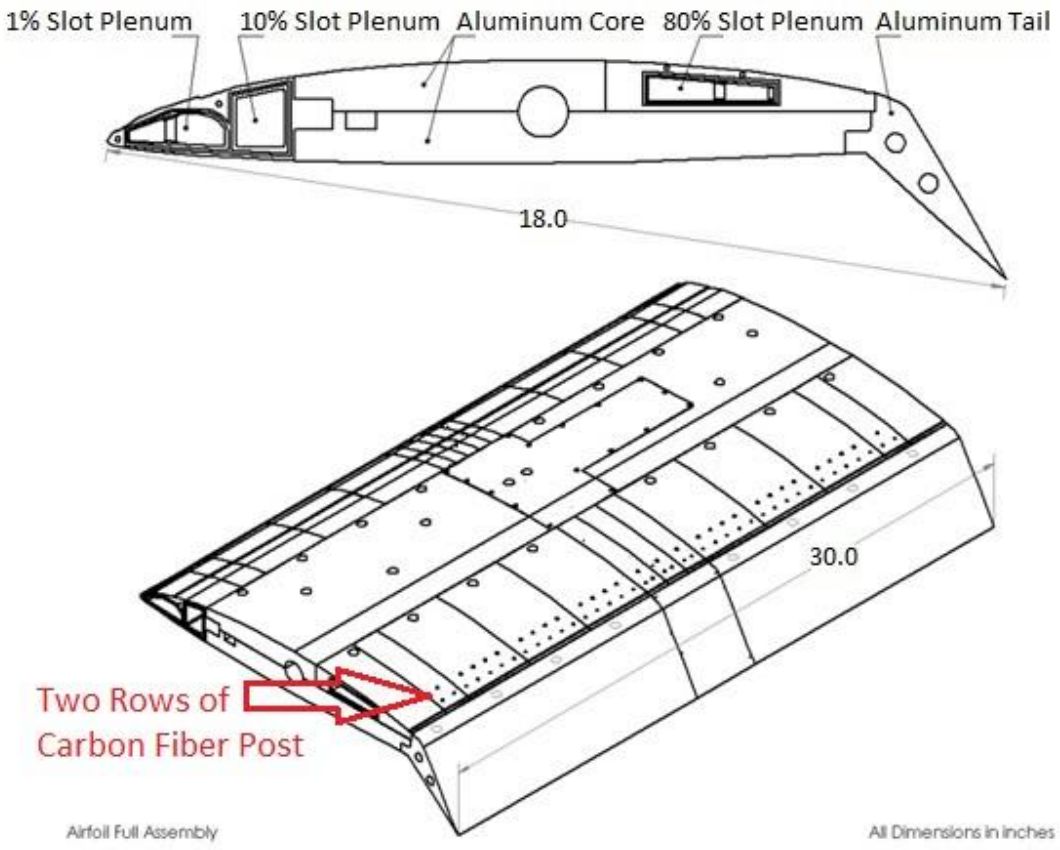

Figure 17. Airfoil profile and assembly

using this 3D printer, intricate geometries of the airfoil and other parts could also be made. Figure 18 shows the detailed geometry of both the leading edge and aft sections. The size of the airfoil and the unique design of the slot plenums require constructing the model in sections. These sections were pieced together to create the full airfoil assembly. Building the model in sections also enable it to be assembled and disassembled repeatedly if any damage were to occur to any of the individual components. To create the entire plenum assembly, 15 and 13 leading edge and aft subsections, respectively, were made and mated together (Figure 17).

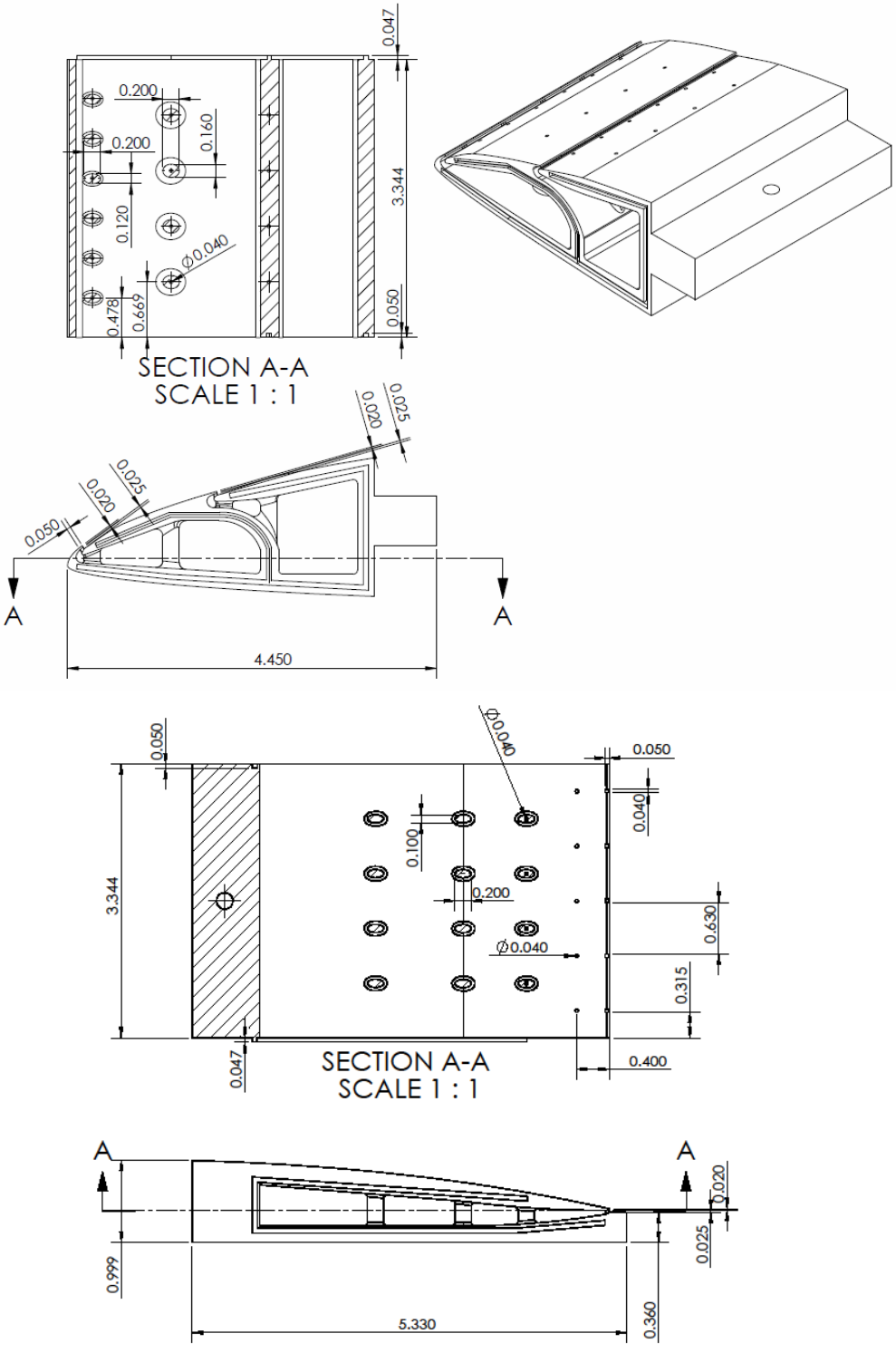

Figure 18. (a) Leading edge, and (b) aft section detail

During testing, air is injected directly into the boundary-layer from the three tangential slots positioned on the upper surface of airfoil at 1%, 10%, and 80% of the non-deflected chord. These steady blown slots span the center 26 inches, with 2 inches on either end not blown. Each slot is independently provided high pressure air from the WiST lab's three auxiliary air tanks. This air is supplied via a 2 inch galvanized iron pipe that is split three ways to feed each plenum (Figure 12b).

To supply each plenum the proper amount of air and maintain the correct back pressures three Parker 53R 1 ¼ inch dial regulators with a range of 0-40 psig and 700 SCFM maximum flow rate were used in conjunction with digital pressure gauges to give a visual pressure reading (Figure 12b). The supply lines reside outside the tunnel, and are attached to the assembly at the base of the tunnel. Each plenum has a unique geometry at its entrance, and in order to feed air smoothly from the supply lines to the plenums required unique adapters (Figure 18). The transition sections of these RP adapters were modeled in SolidWorks, using fifth order polynomials to maintain a smooth transition from the PVC hoses.

The drawings in Figure 18 and the photos in Figure 19 also show the key and keyhole design between adjacent assembly faces. This key design around the plenum profile prevents air leakage between parts. To further prevent air leakage, the keyhole of each part is filled with high vacuum grease before mating surfaces are tightly pressed together.

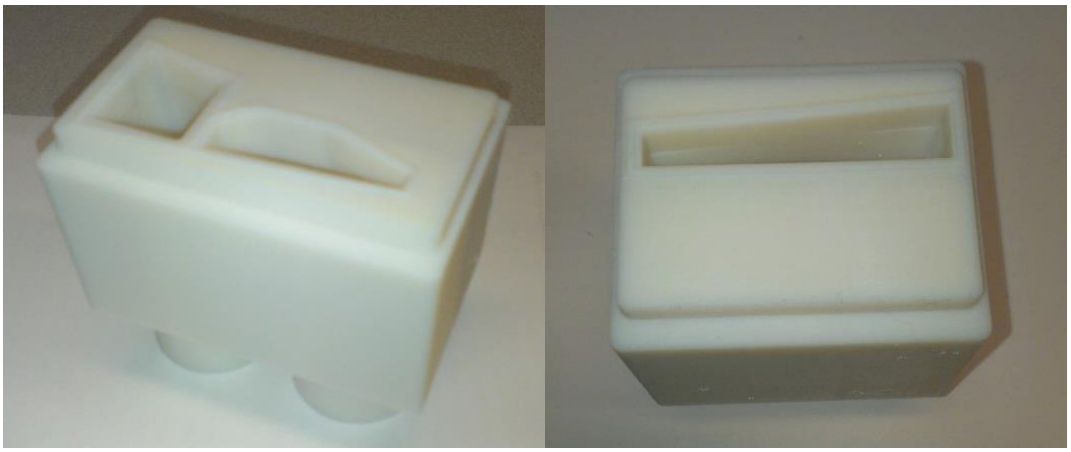

Figure 19. Air feed to airfoil plenum adapters: (a) LE plenums, and (b) aft plenum

The center body of the airfoil is constructed of polished aluminum, and built in two separate sections which enable it to encompass the 1 inch diameter alloy steel rod used to rotate the entire assembly through AoA sweeps. The right and left deflected trailing edge sections are also made from aluminum. These parts are shown below in Figure 20.

Figure 20. Airfoil aluminum: (a) Top and bottom core, and (b) right and left trailing edge

. The aluminum also serves as mating surfaces for all parts made using the 3D printer (pressurized LE and aft plenums, tail section with pressure taps), and has a recess for the ESP scanners to be embedded during testing (Figure 21). The VeroWhite plastic used by the 3D printer is a fairly brittle material. Once the system is pressurized, the high stress levels on the chambers can cause cracks and subsequently failure. This problem is amplified around the slot where the parts are the weakest, and slot integrity is critical. At the slot exit, any variation in slot height can cause the loss of jet uniformity which is key to the success of each test. For these reasons, the plenums were reinforced internally with posts and carbon fiber

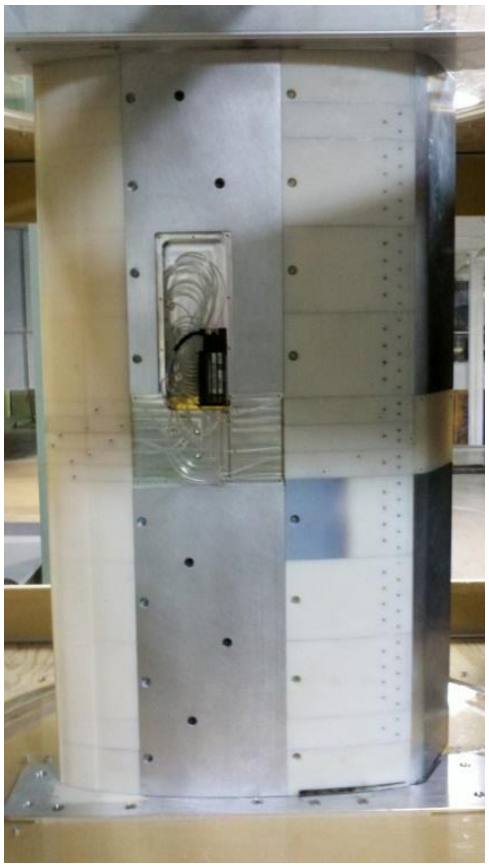

Figure 21. ESP Scanner embedded in airfoil

rods to enhance their strength and enable the parts to withstand the high air pressures and high flow rates. Each slot is also reinforced by thin vertical posts. Figure 21 shows the detailed design of these posts. During initial testing, it was determined that the cantilevered design of the aft section made it uniquely prone to failure once pressurized. To solve this issue, the first two rows of aft plenum post near the slot exit are reinforced with carbon fiber rods. The holes for the rods can be seen in Figures 17, 18, and 21.

Rapid Prototype Post Tensile Tests

Tensile tests were conducted on different post designs using an Instron mechanical testing system. This test was conducted to determine the strength of the VeroWhite posts with and without carbon fiber rods. Figures 22 and 23 show the design of the test samples and a photo of the test samples after production, respectively.

First, a control was established for this experiment by testing a solid VeroWhite post without carbon fiber rods (Figure 22a). Next, three samples were reinforced with carbon fiber rods and epoxy resin (Figure 22b). At the top and bottom of these samples a conical cut is made to give the epoxy resin a larger bonding surface. This test was repeated with .03" and .04" carbon fiber rods to determine the effectiveness of larger carbon fiber rods. Figures 24 and 25 show the final results from these two tests.

The results from both tests show a significant improvement in maximum stress with the addition of carbon fiber posts. On average, there was a 50% and 58% increase in maximum for the .03 and .04 inch carbon rods, respectively. For the final assembly, .03 inch carbon rods were used inside the second row of posts and .04 inch carbon rods were inserted on their own in the first row nearest the slot. By using .04 inch carbon rods without

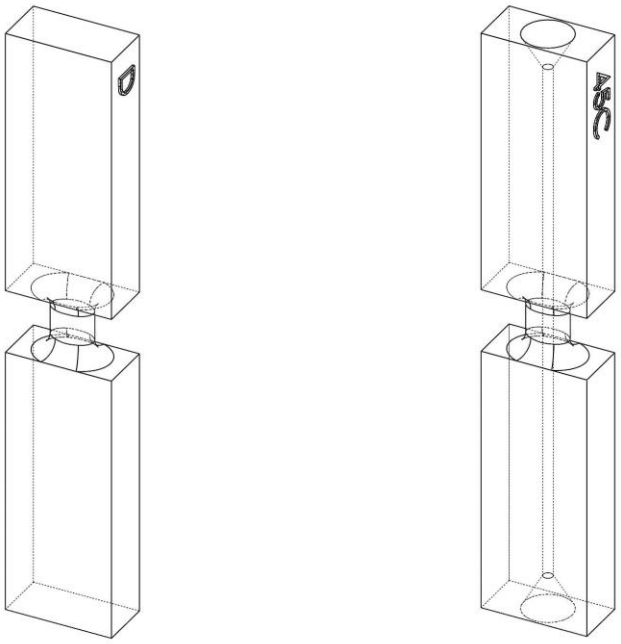

Figure 22. Post test samples: (a) control, and (b) conical w/ carbon fiber rod

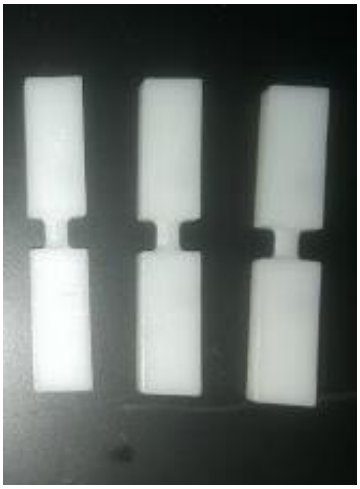

Figure 23. Post production test samples

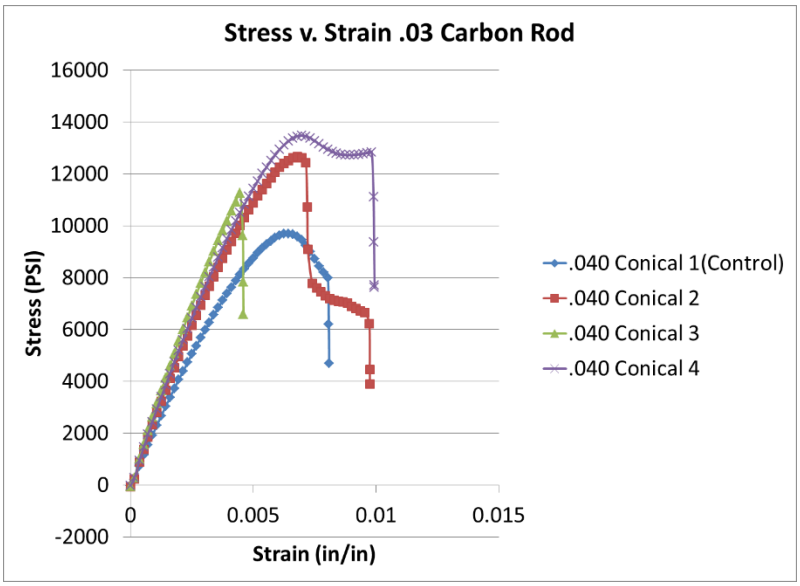

Figure 24. Sample post tensile test (.03 inch carbon fiber rods)

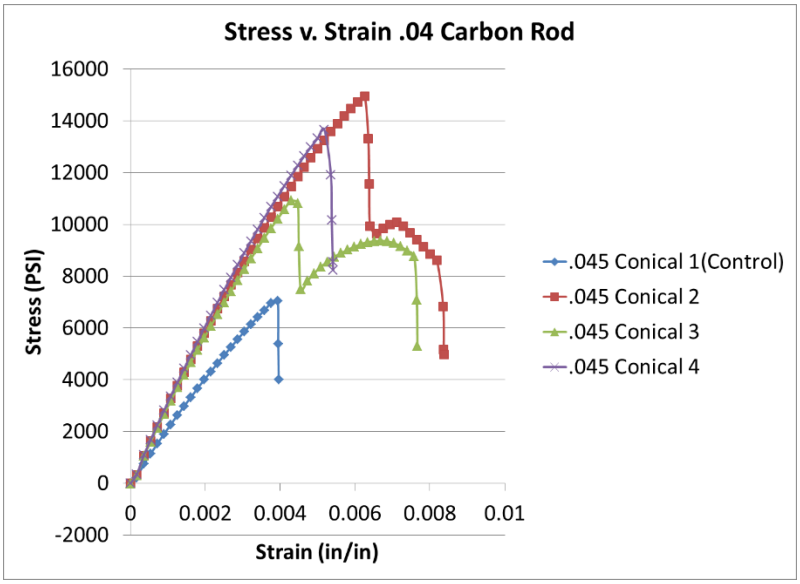

Figure 25. Sample post tensile test (.04 inch carbon fiber rods)

VeroWhite plastic posts near the slot, extra material is eliminated and the rapid prototype cleaning process is simplified.

Pressure Measurement System

Twenty-seven pressure ports are distributed around the airfoil in the center 3 ¼ inches of the span. The location of each pressure port is listed in Table 1. Pressure ports are clustered around the leading edge and the shoulder where the pressure changes are predicted to be the greatest. As previously mentioned, two DTC ESP Scanners were used during testing. The first ESP scanner, embedded inside the airfoil (Figure 20), was connected to the pressure ports located around the airfoil to provide pressure distribution data, while the second was connected solely to the wind tunnel Pitot tube to measure freestream tunnel velocity. Each ESP pressure scanner has 32 ports and each port is connected to its own dedicated pressure transducer. This gives the ability to read pressure at each port simultaneously.

A DTC Initium high speed data acquisition system reads the data from each ESP scanner simultaneously (Figure 26). The data acquisition rate for the DTC Initium was set to 250 Hz and data was collected over 10 seconds. The collected data is then averaged to mitigate time dependent fluctuations in pressure readings. Once the data is acquired, it is converted into C_p measurements using the freestream dynamic pressure.

A MATLAB code (Appendix A) was written specifically for integrating surface pressure distribution ($C_{p)}$ around the airfoil to generate lift and drag coefficient results presented in the following chapter. The C_p values from each pressure port are input into the MATLAB with their know locations and the area between each pressure port is calculated

Table 1. List of pressure port locations (x/c)

upper surface	lower surface
0.03	0
0.06	0.01
0.08	0.03
0.12	0.05
0.15	0.1
0.2	0.3
0.36	0.6
0.5	0.8
0.6	0.94
0.7	
0.75	
0.81	
0.82	
0.84	
0.86	
0.88	
0.9	
0.94	

Figure 26. DTC Initium and ESP Scanners

and converted into corresponding dx & dy values. By averaging the C_p values at the beginning and end of each area, and effective average pressure ($\bar{p}$) over the area between pressure ports can be determined. Multiplying the average pressure with the corresponding x & y components (i.e. dx and dy) gives x & y force components for each area. This method is repeated around the entire airfoil surface. The summation of all x & y forces around the airfoil gives the resultants x & y forces (i.e. N &A). Finally, by taking into account AoA, the resultant forces can be broken down in lift and drag. The equations used for calculation are list as follows:

$$\begin{cases} \bar{p}_i = \frac{1}{2}(p_i + p_{i+1}) \\ \bar{p}_n = \frac{1}{2}(p_n + p_1) \end{cases} \tag{6}$$

$$\begin{cases} dx_i = x_{i+1} - x_i \, , dy_i = y_{i+1} - y_i \\ dx_n = x_1 - x_n \, , dy_n = y_1 - y_n \end{cases} \tag{7}$$

$$N = \sum_{i=1}^{n} \bar{p}_i \, dx_i \tag{8}$$

$$A = -\sum_{i=1}^{n} \bar{p}_i \, dy_i \tag{9}$$

$$L = N * \cos(\alpha) - A * \sin(\alpha) \tag{10}$$

$$D = N * \sin(\alpha) + A * \cos(\alpha) \tag{11}$$

Jet Uniformity

For accurate test results, jet uniformity from the slot exit is critical. Before the model was assembled, jet uniformity was tested outside of the wind tunnel. In the following test, jet uniformity was tested on a 4 inch slot. Pressure inside the chamber was monitored, while pressure along the length of the slot was measured using a small handheld probe. Both the probe and the chamber pressure lines were connected to Mouser 0-100 psig pressure sensors.

Air was fed from the left side of the model and this point is designated 0 inches. Air pressure was regulated to 2 psig. Figures 27 and 28 show the results from this test on both the 1% and 10 slot, respectively.

In both tests, the pressure at the slot exit remains relatively flat and slightly under the value recorded inside the slot plenum. The pressure difference between the slot exit and the plenum is greatest near the air feed entrance, but this difference begins to decline farther from the air feed entrance. In the final assembly, this problem was mitigated in two ways. First, the inserts (Figure 18) connecting the airfoil plenums and the feed lines were designed to prevent choking create a smoother transition for the assembly. Second, two inches on either side of the slot are not open. However, there are still near-wall effects at the edge of the slot.

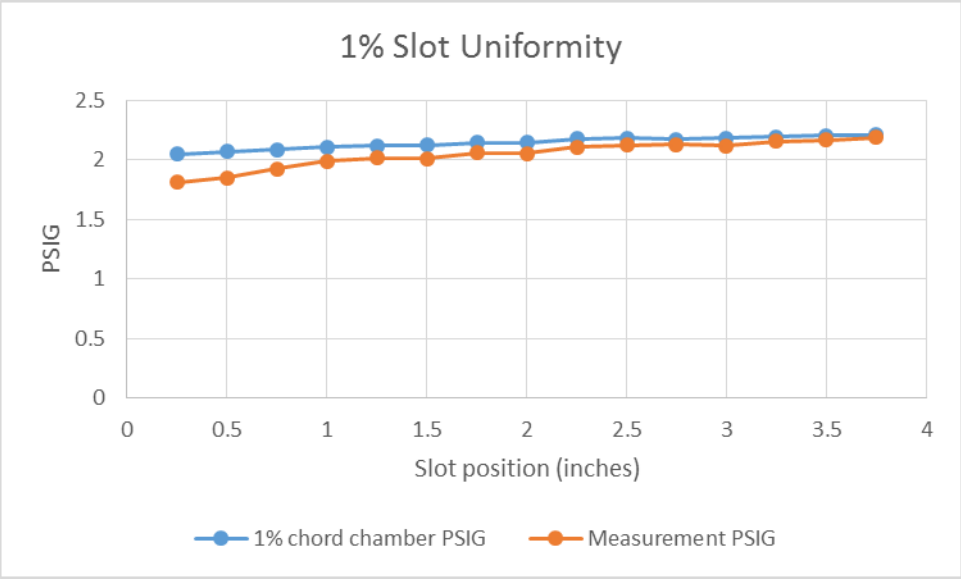

Figure 27. 1% slot uniformity test (4 inch model)

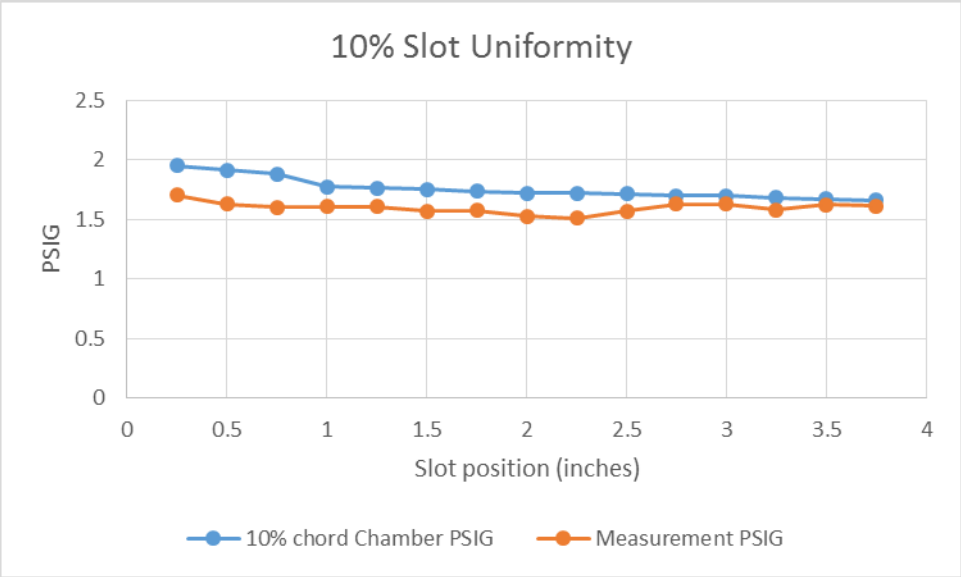

Figure 28. 10% slot uniformity test (4 inch model)

CHAPTER 4. RESULTS

Testing for this study was broken down into 5 different cases: The first case study, without the effects of AFC, is referred to as the "baseline". The next four cases examine AFC effects from each slot with varying values of C_μ. In between each run and before changing AoA, the tunnel was turned off to prevent unnecessary loading on the motor. For each case, data was taken between 0 and 10 degrees AoA.

Steady Blowing Results

The baseline case was established for the airfoil by the sealing over all three slots with 2.2 mm thick Mylar tape. This tape was then removed for subsequent steady blowing tests. Data was then collected at two freestream dynamic pressures (q_∞=30 psf and 20 psf), the results of which are analyzed and compared in this chapter. Table 2 shows the freestream dynamic pressure verse the chord Reynolds number. For each AFC case, nominal C_μ values were chosen based on the previous work done by Bright (2012) (Table 3).

Table 2. Dynamic pressure and Chord Reynolds number

Q∞ (psf)	Reynolds Number
30	1.44E+06
20	1.15E+06

Table 3. C_u values at each slot location for all 5 cases

	$C_{\mu,1}$	$C_{\mu,2}$	$C_{\mu,3}$
Baseline	0	0	0
Blown Flap	0	0	0.040
LE Blowing	0.065	0	0.040
Equal Blowing	0.065	0.065	0.040
Unequal Blowing	0.065	0.130	0.040

Figures 29 and 30 show the lift vs. angle of attack data of all five cases for q_∞=30 psf and q_∞=20psf, respectively. For all cases, AFC was able to improve maximum lift over the baseline deflected flap results. When both LE slots are turned on (i.e. Equal and Unequal blowing), the greatest improvements in lift are seen. For example, the Unequal blowing case, shows the greatest lift improvement over the baseline results for both q_∞ = 30 psf & 20 psf. from both LE slot slots also increases the stall angle in comparison to the other AFC cases. Stall occurs around 4 degrees for both the blown flap and LE blowing cases, while stall has been increased to approximately 8 degrees for the Equal and Unequal blowing cases. At Applying AFC lower speed, the effects of AFC on lift enhancement are more pronounced.

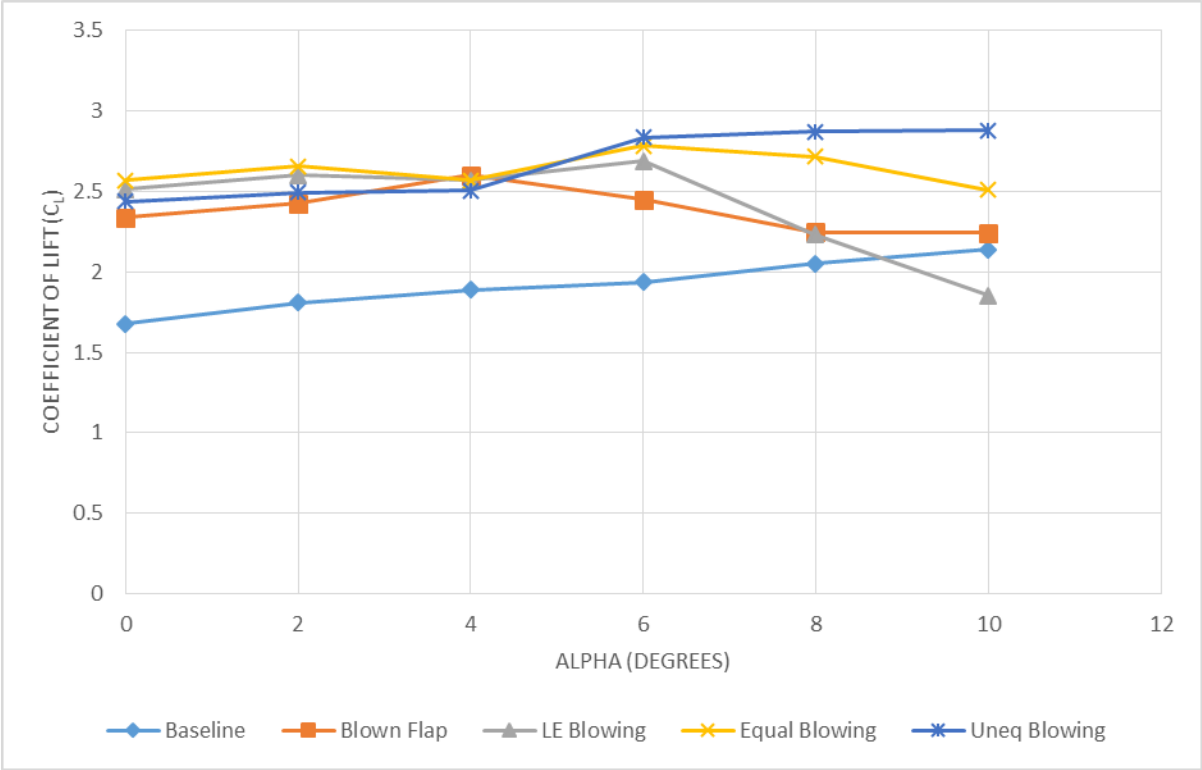

Figure 29. Lift vs. AoA for all 5 cases (q_∞ =30 psf)

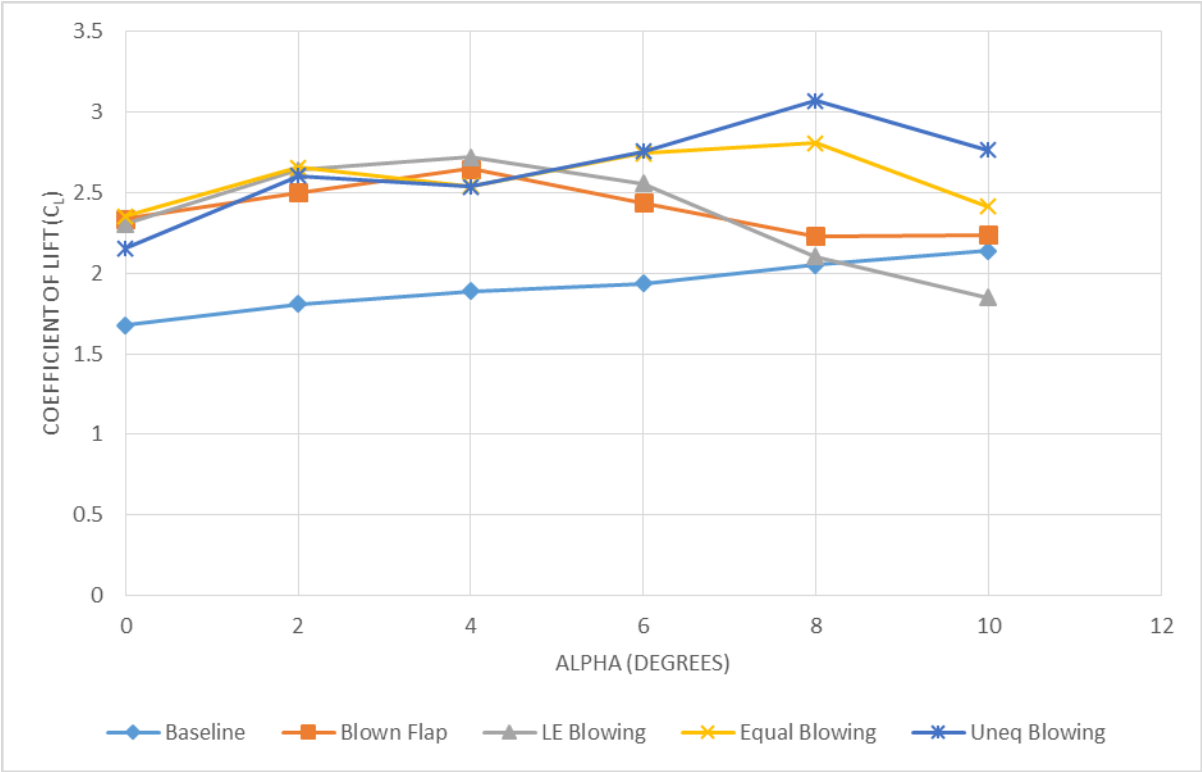

Figure 30. Lift vs. AoA for all 5 cases (q_∞ =20 psf)

For example, the percent increase in lift, for the Unequal blowing cases, is 31% and 43% for q_∞=30 psf and q_∞=20psf, respectively. These results are shown in further detail in Table 3. The lift improvement is good, but under the anticipated 100% lift improvement seen by Bright (2012). The cause of this will be examined in further detail in subsequent sections.

Figures 31 and 32 show the drag vs. angle of attack data of all five cases for q_∞=30 psf and q_∞=20psf, respectively. When comparing the lift and drag plots v. AoA, there are a few noticeable trends. First, LE blowing, Equal blowing, and Unequal blowing all show a slight reductions in drag at 0 degrees in comparison to the baseline. This is consistent for both freestream dynamic pressures. For all cases the drag curves between approximately 0-4 degrees are very similar, showing a roughly linear increase in drag. After 4 degrees, each

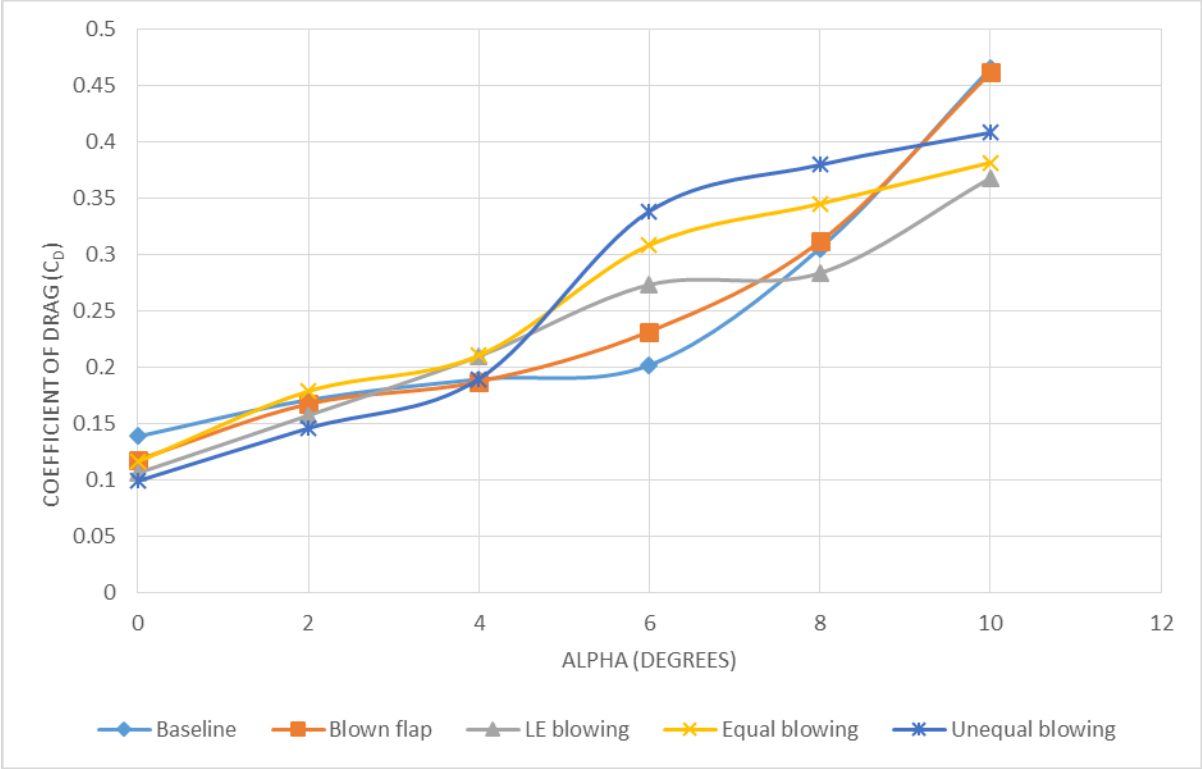

Figure 31. Drag vs. angle of attack for all 5 cases (q_∞ =30 psf)

curve beings to fluctuate more uniquely. There is dramatic increase in drag between 4 and 6 degrees for the LE blowing, Equal blowing and Unequal blowing cases. This increase in drag coincides with continued increases in lift, and therefore is an effect of increased lift-induced drag, which is proportional to the square of lift. However, in each of these particular cases drag begins to level off, directly after the jump, as maximum lift is achieved. This is an indication of loss of lift due to separation, but could also be a sign of near-wall tunnel effects. This is also consistent for both freestream dynamic pressures. Finally, for both freestream dynamic pressures, the blown flap and baseline drag curves are almost identical between 0-

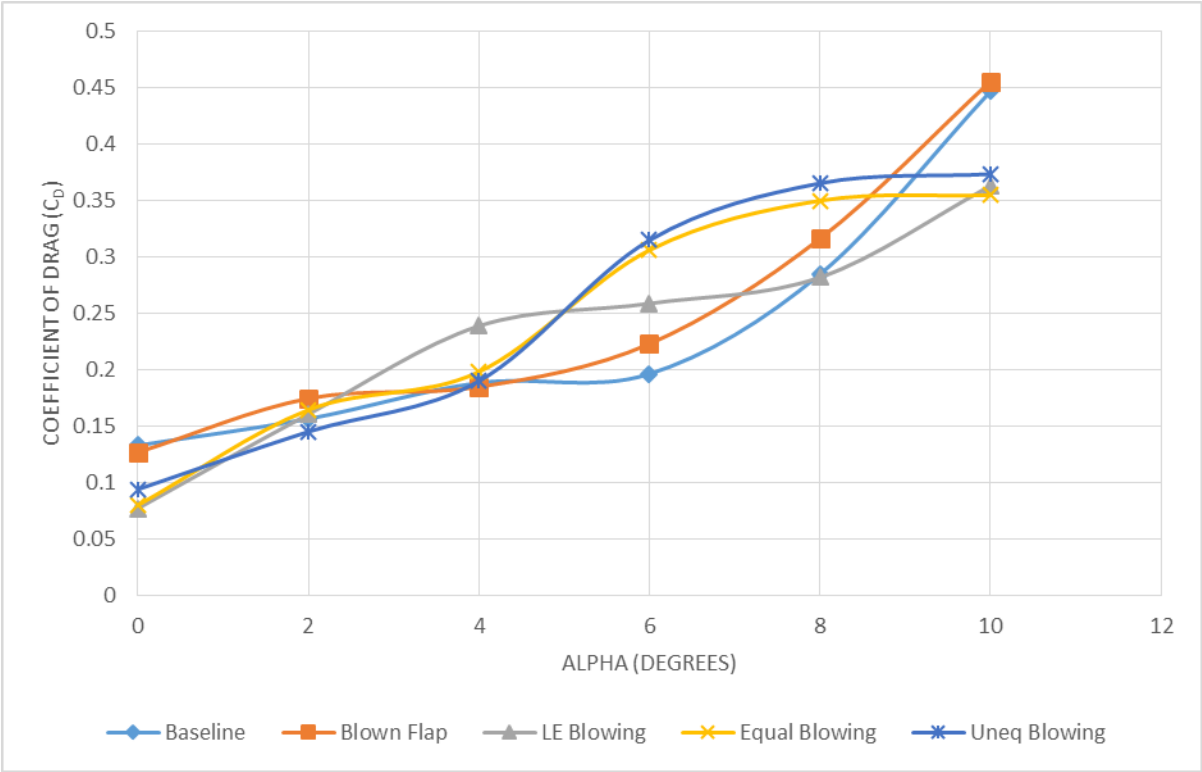

Figure 32. Drag vs. angle of attack for all 5 cases (q_∞ =20 psf)

10 degrees. Higher lift for the blown flap case leads to higher drag, but as AoA is increased passed 4 degrees and the effects of the blown flap are lost, the drag curves for the blown flap and the baseline begin to line up. For q_∞ = 30 psf, these two curves become indistinguishable after 8 degrees.

Table 4. C_L improvements over baseline for steady blowing cases (q_∞ = 30psf & 20psf)

	Q=30psf			Q=20psf		
	$C_{L,max}$	ΔC_L	%increase	$C_{L,max}$	ΔC_L	%increase
Baseline	2.19	0.00	0.0	2.14	0.0	0.0
Blown Flap	2.60	0.41	18.6	2.65	0.51	23.7
LE Blowing	2.69	0.49	22.5	2.72	0.58	27.0
Equal Blowing	2.79	0.59	27.0	2.81	0.67	31.2
Unequal Blowing	2.88	0.69	31.3	3.07	0.93	43.4

Effects of Freestream Velocity

Varying freestream velocity had an effect on lift as previously mentioned. At the lower speed case, lift improvements were higher but the trends and stall angles for each case are very similar. It should also be noted that although the lift gains are higher for lower freestream velocity, the maximum lift ($C_{L,max}$) for each case is approximately equal.

The trends in the steady blowing lift curves are very consistent at both freestream dynamic pressures. For example, at both freestream pressures, $C_{L,max}$ for the blown flap case is achieved at 4 degrees, where the airfoil begins to stall and lift drops off steadily. This low stall angle and steady drop in lift is as expected, and is consistent with the findings of Pfingsten (2005), Burnazzi (2013), and Bright (2012). The blown flap is only providing marginal lift improvements at 10 degrees AoA. For the LE blowing case, stall angle is approximately the same for both freestream velocities, 4 and 6 degrees for q_∞ = 20 psf and 30 psf, respectively. In this range, the lift curve is fairly flat. After 6 degrees, there is a sharp drop off in lift and by 10 degrees lift is under the baseline value. The Equal blowing case, like the LE blowing case, appears to stall around 6 degrees AoA, but the effects of stall are milder and the airfoil is still producing more lift than the baseline at 10 degrees. For both freestream velocities, the Unequal blowing case produces the highest amount of lift. Maximum lift occurs at 8 and 10 degrees for q_∞ = 20 psf and 30 psf, respectively. For q_∞ = 20 psf, lift begins to drop after 8 degrees indicating stall, however, for q_∞ = 30 psf this drop in lift has not been seen yet.

The trends found in Figures 29 and 30 are not far from what was seen by Bright (2012), and the stall angles for each case vary only slightly. However, the maximum lift for

all the cases with leading edge blowing is much less than anticipated. To gain further insight the pressure distributions are analyzed in the following section.

Pressure Distribution Analysis

The following section is broken into two parts. First, the pressure distributions of all cases at q_∞ = 30 psf & 20 psf are examined and compared in detail. These pressure distributions show that the airfoil was successful in generating high-lift around the LE. Second, select pressure distributions for LE blowing, Equal blowing and Unequal blowing cases at q_∞ = 30 psf were then chosen to demonstrate the problems around the shoulder of the deflected flap. The obstacles shown in each of these cases can be seen in all of other cases at varying levels. Blown flap data was excluded in this part since this is also considered Coanda blowing, the effects of which are highly documented. For each figure in this part, AoA's were chosen for pre and post stall conditions.

Figures 33 and 34 show the baseline pressure distributions for the airfoil. The baseline airfoil continues to generate lift until 10 degrees due to the high-speed flow around the laminar LE, indicated by the large LE pressure drop (i.e. more negative C_P values). At 4 degrees, the pressure drop at the leading edge is greatest, but at 10 degrees this pressure drop has diminished. This maximum pressure drop at the LE around 4 degrees will be shown to be consistent throughout testing. This pressure peak at the leading edge is important because it indicates the angle where lift is highest around the leading edge. In each of these figures for the baseline airfoil, there is little no variation over the latter half of the airfoil pressure distribution. Without AFC, the back half of the airfoil has effectively stalled even at 0 degrees. Although the airfoil continues to produce higher lift as AoA increases, the very flat

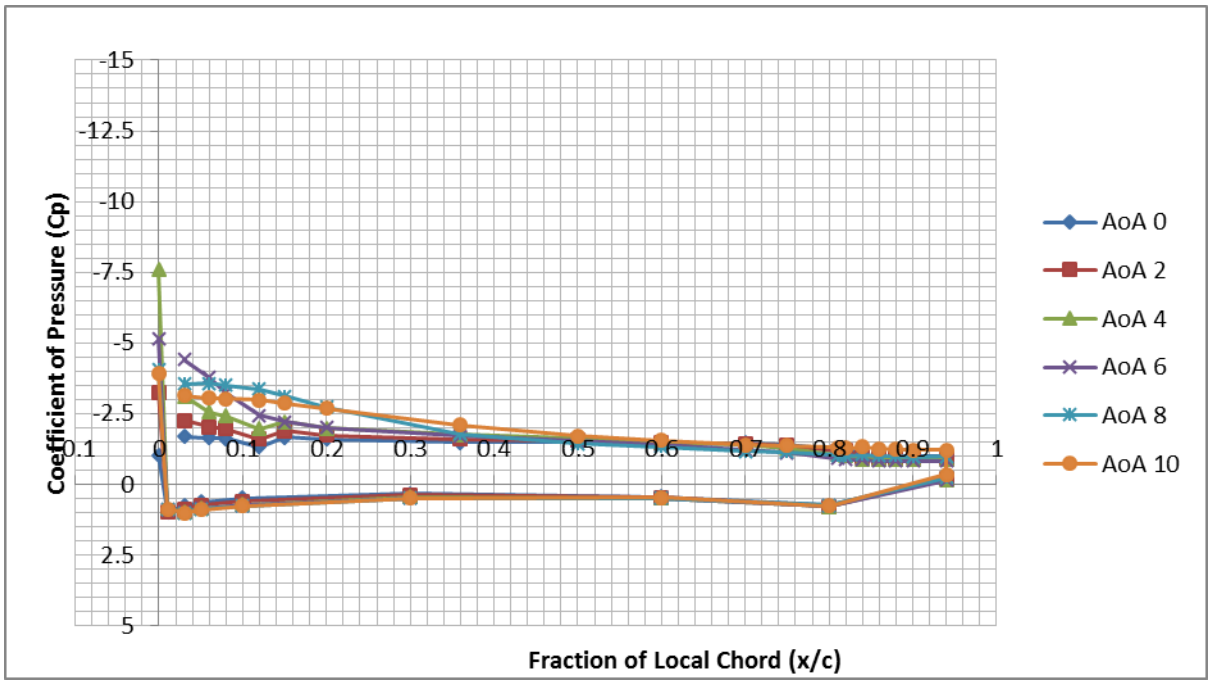

Figure 33. Pressure distributions for Baseline case (q_∞ = 30psf, AoA 0-10)

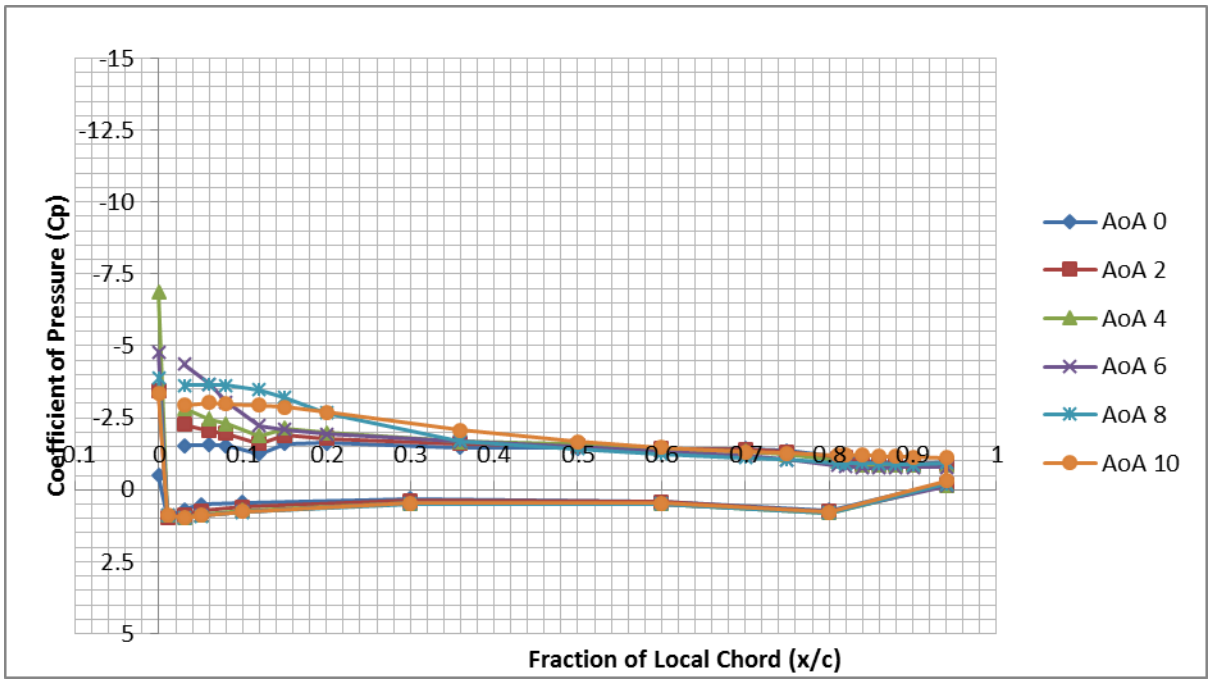

Figure 34. Pressure distributions for Baseline case (q_∞ = 20psf, AoA 0-10)

pressure distribution over the last half of the airfoil indicates that the flow around the tail of the airfoil is separated.

Figures 35 and 36 show the pressure distributions for the blown flap data. The addition of trailing edge blowing is effective in increasing the lift and the pressure drop around shoulder of the airfoil. However, the leading edge is still much more effective in generating high-lift than the shoulder. The most negative pressure peak comes at 2 degrees at the LE for both q_∞ = 30 psf & 20 psf, while the most negative pressure peak around the shoulder comes at 4 and 0 degrees for q_∞ = 30 psf & q_∞ = 20 psf, respectively. For q_∞ = 20 psf, the C_P values around the shoulder are greater than those seen in the q_∞ = 30 psf case. This corresponds to a slightly larger maximum lift for the q_∞ = 20 psf case. However, for both dynamic pressures the flap is in deep stall by 6 degrees.

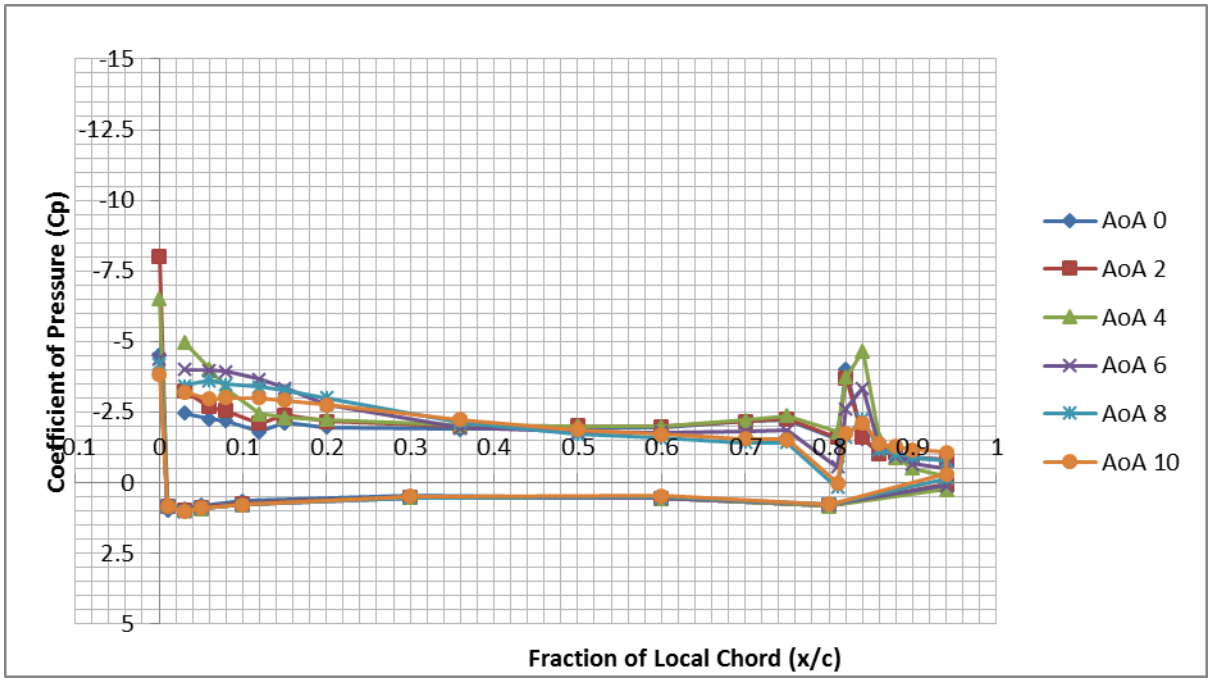

Figure 35. Pressure distributions for Blown Flap case (q_∞ = 30psf, AoA 0-10)

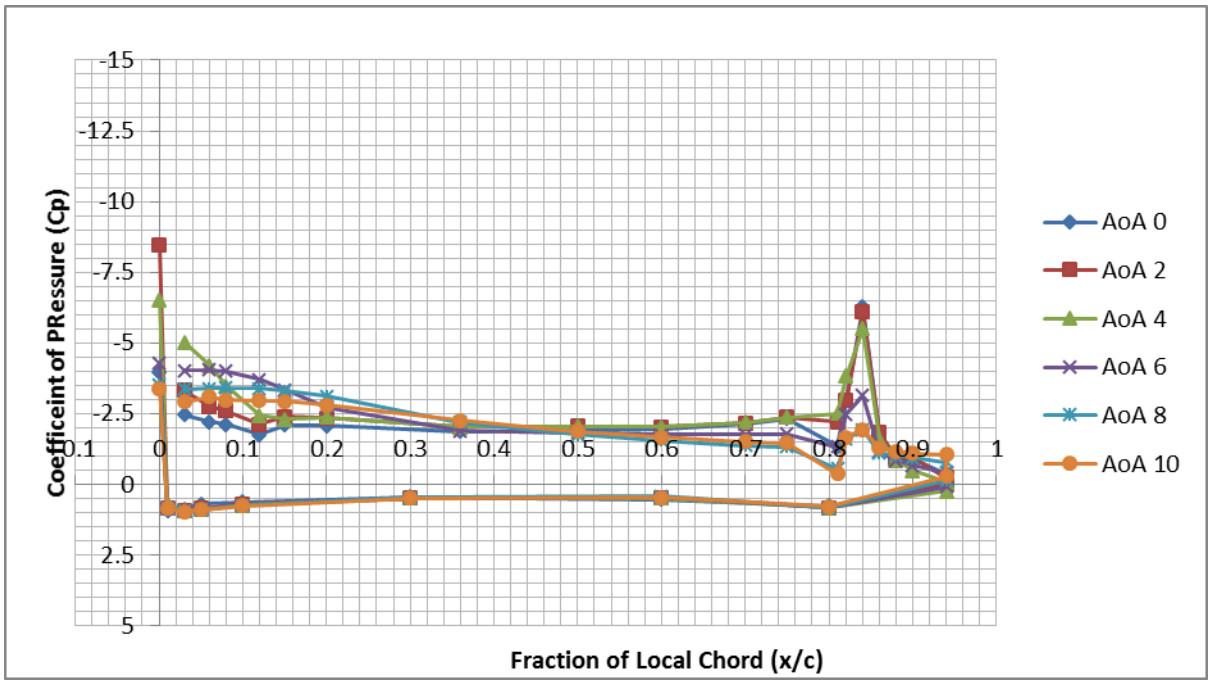

Figure 36. Pressure distributions for Blown Flap case (q_∞ = 20psf, AoA 0-10)

Figures 37 and 38 show all the pressure distributions for LE blowing. The addition of blowing from the 1% slot greatly increases the lift around the leading edge. Specifically, the pressure drop at the LE has increased dramatically. For the blown flap case, the lowest C_P value around the leading edge was approximately -8. For the LE blowing case the most negative leading edge C_P has dropped below -13. This leading edge peak occurs at 4 degrees again for both freestream dynamic pressures. However, this does not lead to a significant increase in lift over the blown flap case. The pressure peak around the deflected flap, seen in Figure 36, is not present at the same level for the LE blowing case. The pressure around the deflected flap is flat, an indication of separation. This separation is preventing a proper Coanda effect, and results in less negative pressure peaks around the shoulder than anticipated. When the Coanda effect is working properly the pressure peaks around the LE

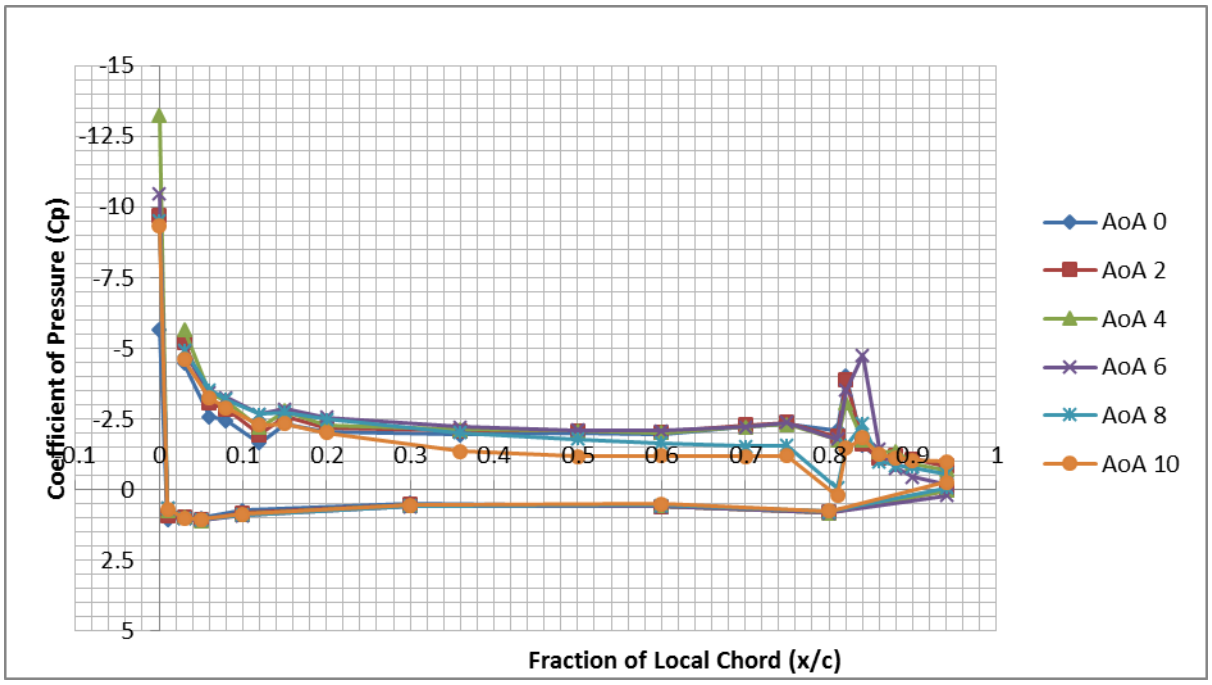

Figure 37. Pressure distributions for LE Blowing case (q_∞ = 30psf, AoA 0-10)

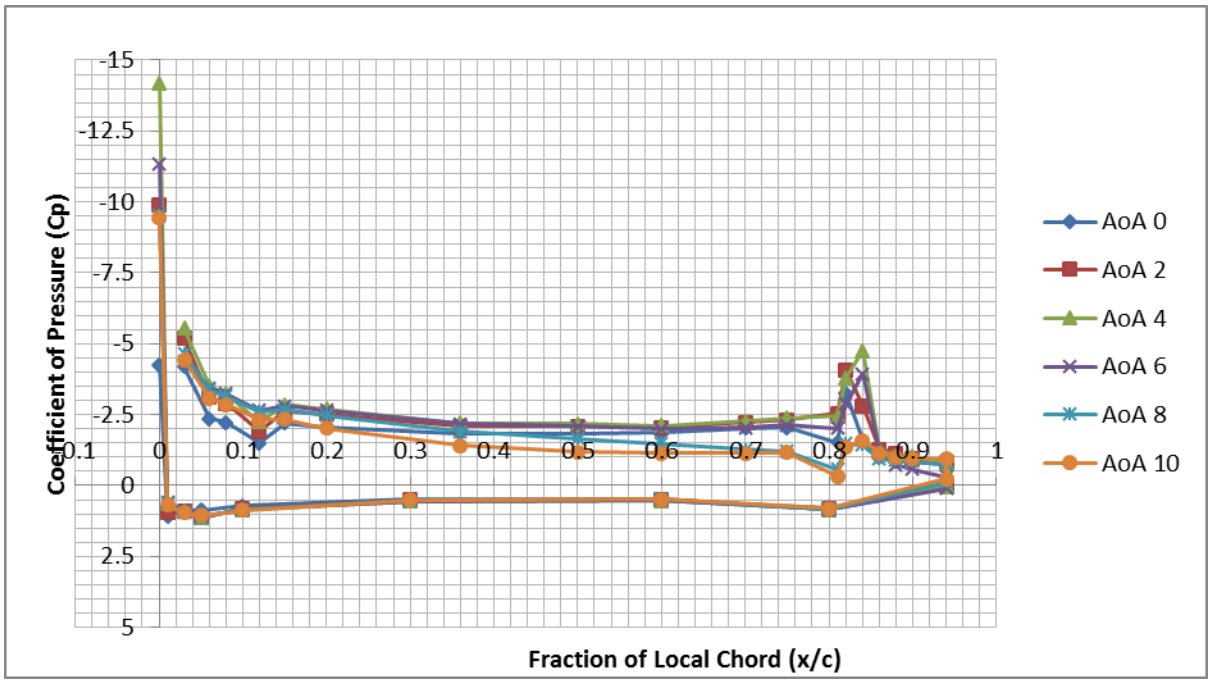

Figure 38. Pressure distributions for LE Blowing case (q_∞ = 20psf, AoA 0-10)

and the shoulder can be of equal magnitude. This is seen in the studies by both Burnazzi (2012) and Bright (2012).

maximum lift and higher stall angles.

The trailing edge continues to stall, but the addition of AFC from the 10% slot does help mitigate separation around the flap. For LE blowing, the trailing edge edge peak is lost by 8 degrees. In the Equal blowing case, the trailing edge peak has reduced but is still present between 8-10 degrees. Figures 39 and 40 show the pressure distributions for the Equal blowing cases. In these cases, both the 1% and 10% slot apply AFC at approximately equal C_μ values. Once again the lift generated around the leading edge is much greater than the lift seen around the shoulder. The addition of the 10% slot leads to a significant increase in flow speed around the leading edge. By comparing the Equal blowing case with LE blowing case, a noticeable negative shift in C_P values can be seen between 0-20% chord on the suction side of the airfoil. The most negative leading edge C_P value occurs at 4 degrees again, however, lift does not drop off after this point. Instead, the suction side pressure values between 0-20% chord continue to become more negative as AoA is increased, and therefore the lift around the leading edge is higher. This leads to higher

Figures 41 and 42 show the pressure distributions for Unequal blowing. Here the C_μ value for the 10% slot is twice that of the 1% slot. As previously stated, this was the most successful case. Once again, the most negative leading edge C_P value occurs at 4 degrees, and reaches values of approximately -14 for both freestream dynamic pressures. The additional flow from the 10% slot leads to significant lift gains around the leading edge. For example, at 10 degrees the peak is no longer at the leading edge and has shifted to 3% chord.

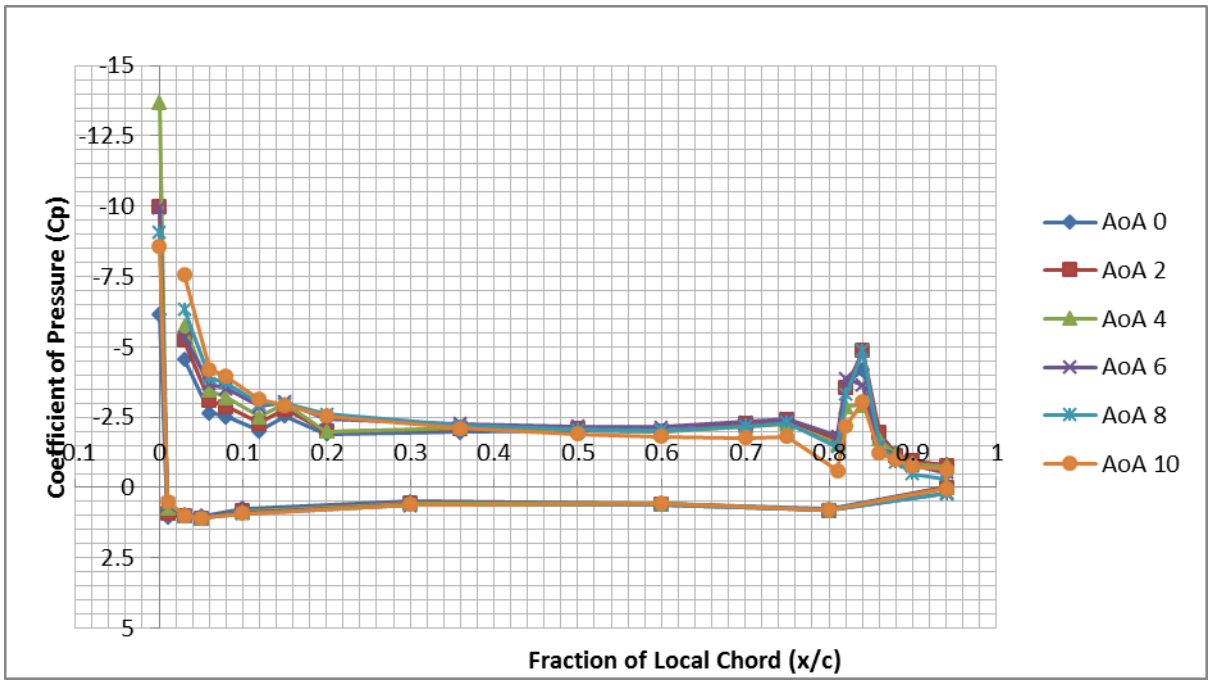

Figure 39. Pressure distributions for Equal Blowing case (q_∞ = 30psf, AoA 0-10)

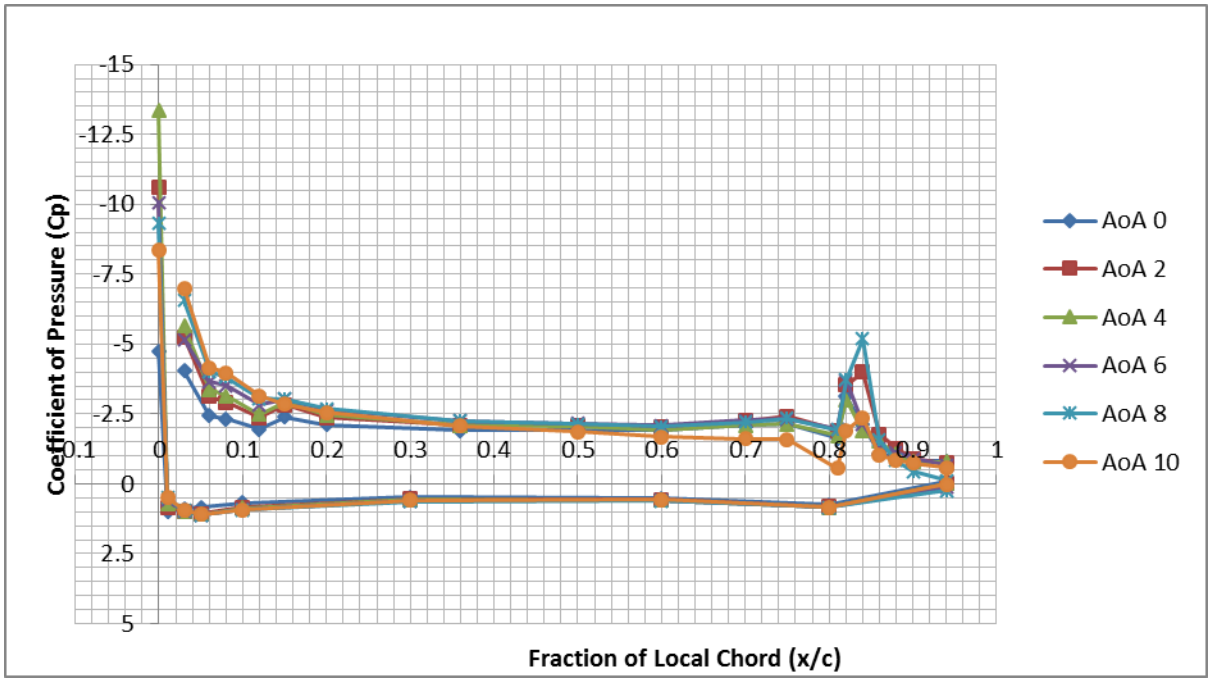

Figure 40. Pressure distributions for Equal Blowing case (q_∞ = 20psf, AoA 0-10)

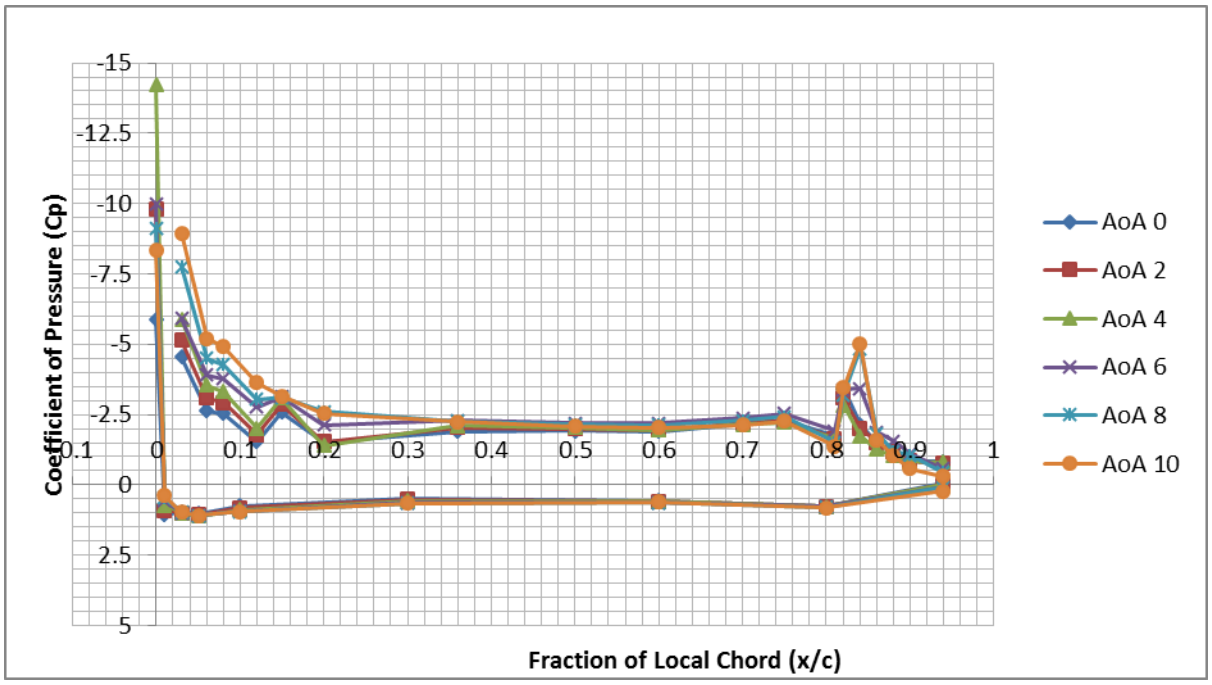

Figure 41. Pressure distributions for Unequal Blowing case (q_∞ = 30psf, AoA 0-10)

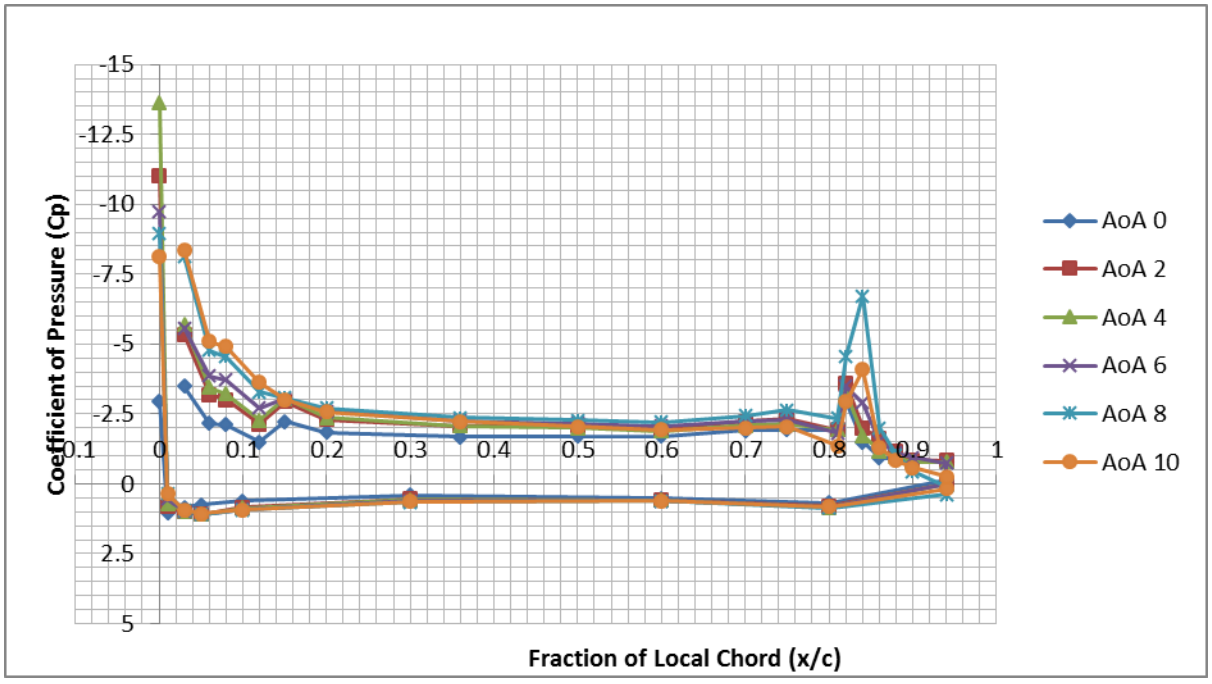

Figure 42. Pressure distributions for Unequal Blowing case (q_∞ = 20psf, AoA 0-10)

This is the only blowing case where this is seen. This increase in leading edge lift results in the highest stall angles and highest maximum lift.

The trailing edge peak is still minimal in comparison the leading edge, but it is at high level in comparison to the previous AFC cases, which is an indication that separation has been further mitigated. At 8 degrees for q_∞= 20 psf, the most negative trailing edge C_P values reaches -6.7 before dropping. Finally, the pressure around the trailing edge is not flat, a further indication of delayed separation.

In each of the previous cases, the lift around the deflected flap of the airfoil is under anticipated. Figures 43, 44, and 45 are used to analyze the problems occurring around the deflected flap for the LE blowing, Equal blowing, and Unequal blowing q_∞= 30 psf cases.

Figure 43 shows select pressure distributions for the LE blowing case between 4-8 degrees. Although momentum is being added from the slot at 80% chord, the pressure at 81% chord is still stagnating despite this momentum addition. By 8 degrees, the pressure at 81% is the highest pressure on the suction side of the airfoil. This is a major problem since pressure stagnation at this location is an indication of separation. Between 4 degrees and 8 degrees AoA, the shoulder pressure peak moves backward from 82% to 84% chord and then drops off at 8 degrees. In the numerical simulation by Burnazzi (2013), much lower pressure peaks around the shoulder are predicted. This pressure drop over the shoulder is caused by the Coanda effect. The Coanda effect states that the flow from the jet wants to stay attached to the adjacent wall, and in order to that it must accelerate over the shoulder. This flow acceleration causes a sharp drop in pressure, and additional BL energy enable it to stay attached until the trailing edge. Since this is not seen in Figure 43, it is highly likely separation has occurred and is preventing the Coanda effect.

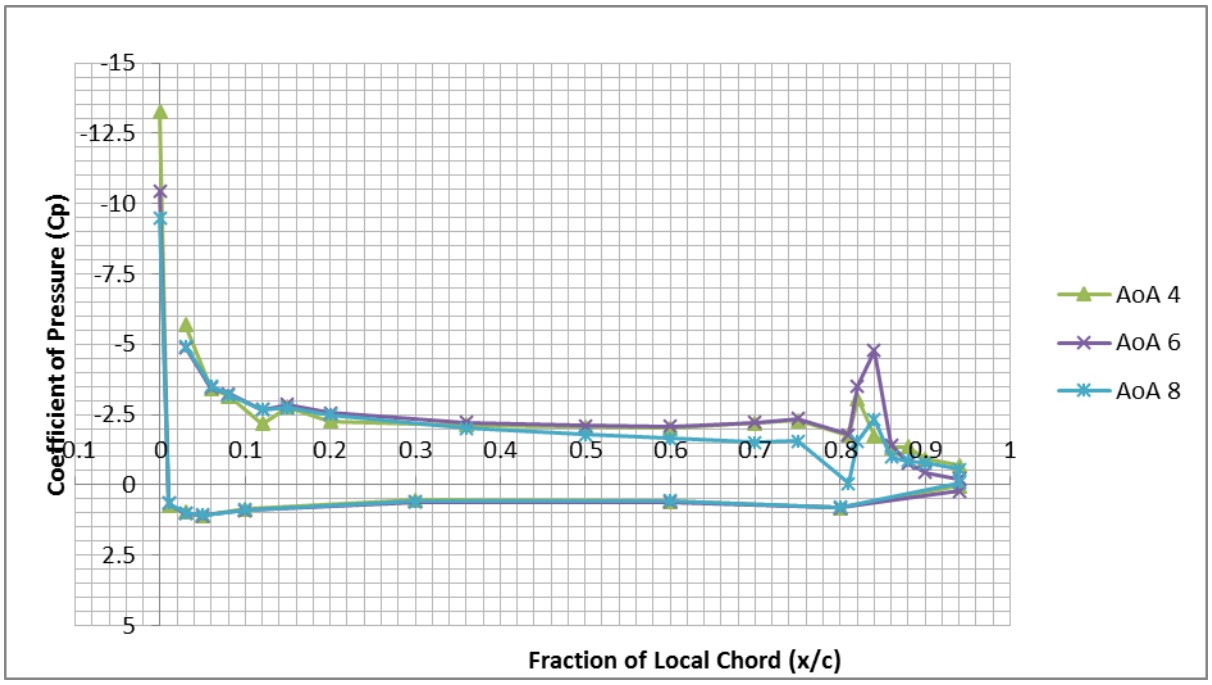

Figure 43. Pressure distributions for LE blowing case, q_∞= 30 psf (AoA 4-8)

There is also an obvious leveling off of pressure around the tail of the airfoil. This is a further indication of full separation over the tail of the airfoil, which is confirmed by the reduction in lift in Figure 29.

Figure 44 shows select pressure distributions from the Equal blowing case between 6-10 degrees. Similar to the LE blowing case, the shoulder C_P values are not as negative as anticipated, and the pressure at 81% chord is high despite the momentum addition from the slot. Again, the pressure at 81% is high, but has not risen to level seen in the LE blowing case, which indicates the addition of momentum for the 10% slot is having an effect. At 8 degrees for the LE blowing case, C_p is approximately equal to 0. At the same point and AoA for the Equal blowing case, C_p equals -1.4 and has not increased to 0 by 10 degrees. This is positive, as it shows the additional blowing does increase the peak value over the shoulder.

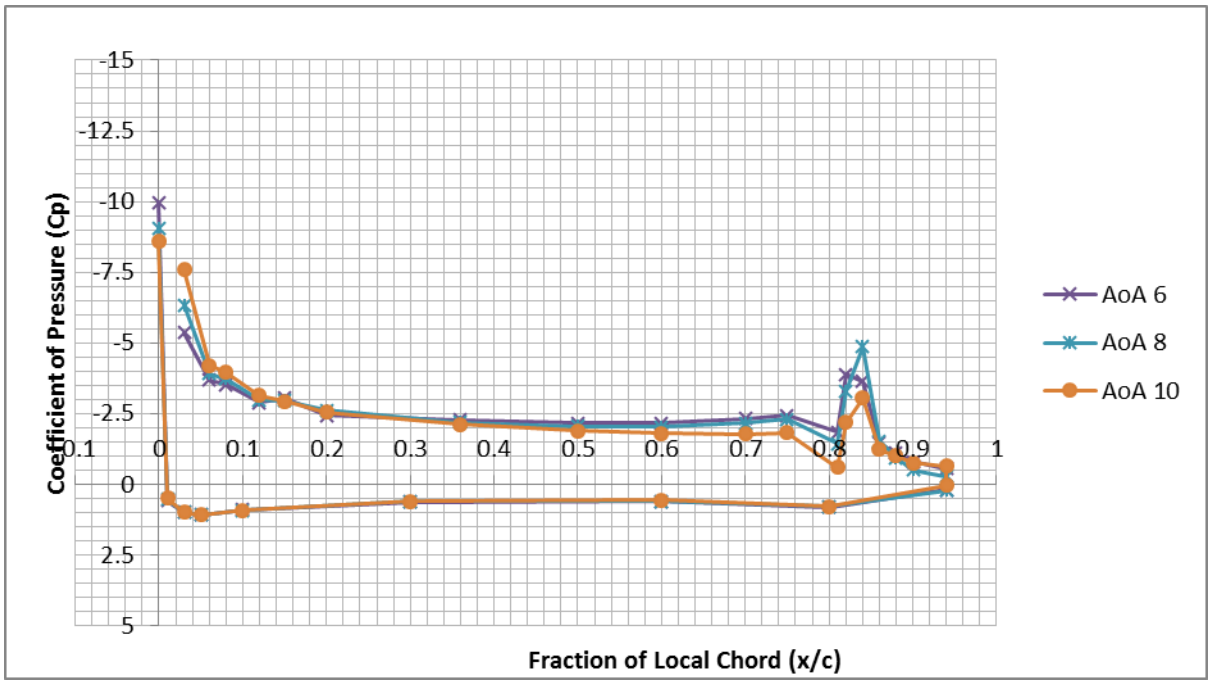

Figure 44. Pressure distributions for Equal blowing case, q_∞= 30 psf (AoA 6-10)

However, Figure 44 still shows further indications of separation around the tail of the airfoil. The low pressure peak starts off at 82% chord, moves to 84% chord, and then drops. At the same time, the pressure at the trailing edge of the airfoil, after 86% chord, has leveled off again.

The Unequal blowing case is the only one that has yet to see a significant drop in lift by 10 degrees, but this is due in most part to the high-lift generated by the leading edge. Figure 45 shows select pressure distributions from the Unequal blowing case between 6-10 degrees. The maximum lift in this case is still lower than anticipated, but definite improvements have been made in the pressure distribution. Both the low pressure peak at shoulder (C_p=-5, AoA=10) and the pressure at 81% chord (C_p=-1.4, AoA =10) are at their lowest levels. The additionally momentum from the 10% slot has reduced the level of

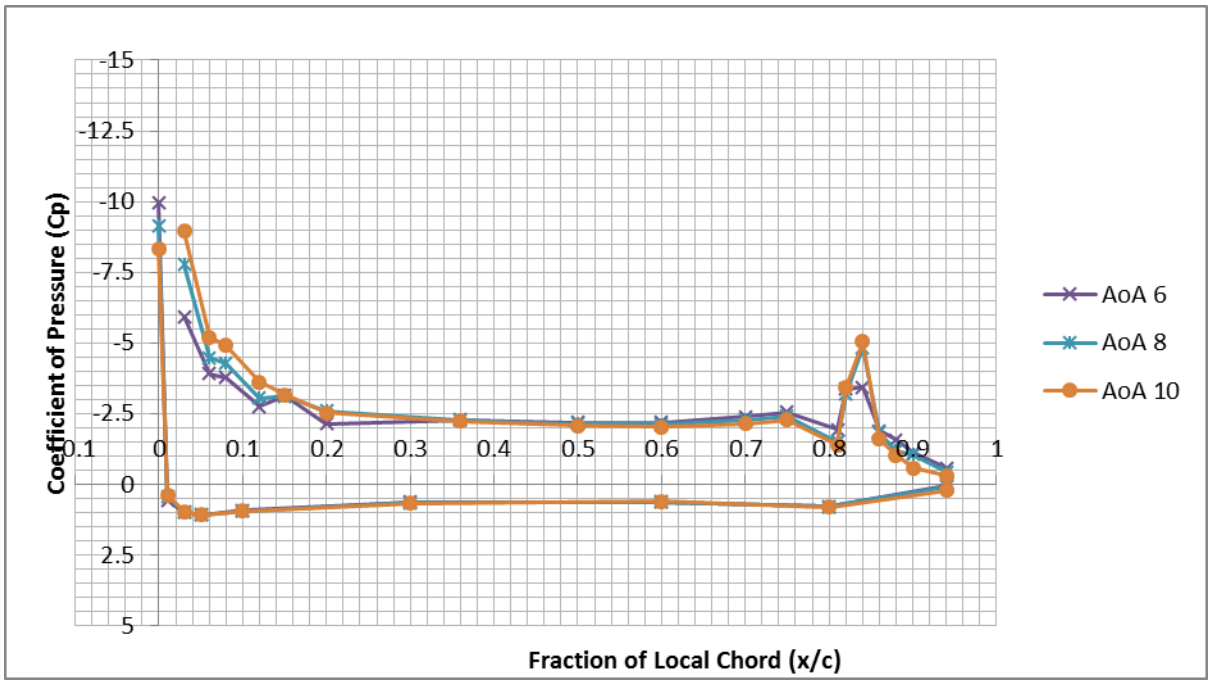

Figure 45. Pressure distributions for Unequal Blowing case, q_∞= 30 psf (AoA 6-10)

stagnation at 81% chord and improved the Coanda effect over the shoulder. The pressure distribution over the tail of the airfoil shows a more gradual increase as it reaches the trailing edge, and the low pressure peak at 84% chord is still present at 10 AoA. These two factors indicate that separation has been delayed or mitigated over the trailing edge.

The pressure distributions for each of these steady blowing cases indicate that the airfoil is unable to overcome the adverse pressure gradients around the tail. This adverse pressure gradient indicate the airfoil is stalled, where low pressure peaks should be more negative as the flow accelerates around the shoulder of the deflected flap. In cases such as LE blowing and equal blowing, this adverse pressure gradient leads to full separation over the deflected flap. Without a proper Coanda effect around the shoulder, the overall lift enhancement produced by AFC becomes much lower than predicted by Bright (2012).

Error Analysis

Each of the calculations performed in this study come with a certain amount of uncertainty due to error from instrumentation and limitations of the test set-up. This section addresses the uncertainty in both the C_μ calculations and the C_L and C_D calculations.

C_μ values are based upon the pressure supplied to each plenum which is controlled by the three 53R Parker dial pressure regulators. These pressure values have been back calculated from the desired C_μ values. However, the pressure from the regulators is not constant and fluctuates with time. As mentioned previously, to get more accurate readings from the dial regulators, digital pressure gauges were installed onto the pressure regulators. The pressure from two dial regulators was monitored over a 2 second period. Figure 46 shows the pressure variance from the two regulators. Both regulators have an average pressure variance of ±.20 psig. Since C_μ is also dependent on freestream dynamic pressure, this pressure change from the regulators gives a different uncertainty level for each

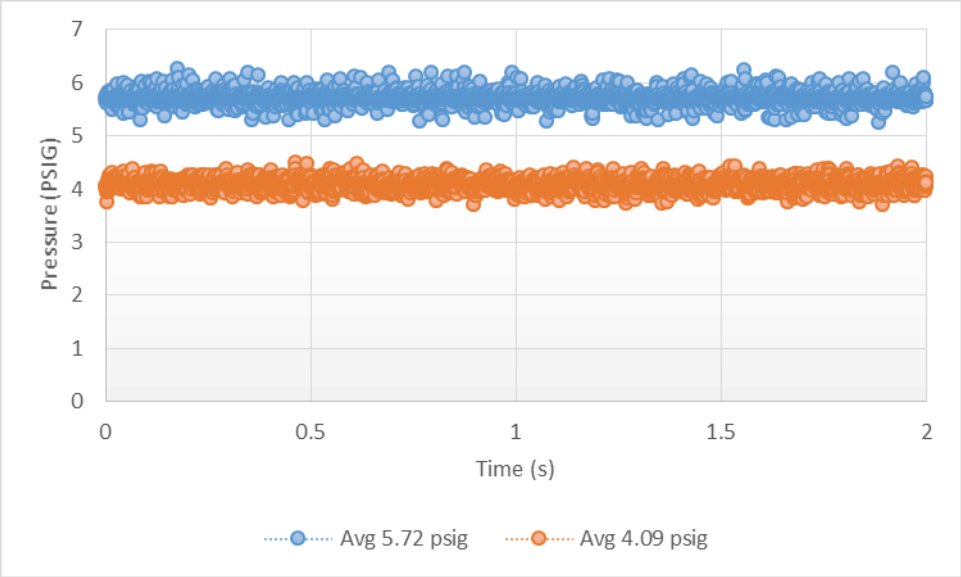

Figure 46. Dial regulator pressure variance over time

freestream dynamic pressure. From this data, C_μ uncertainty is estimated at ±.003 and ±.002 for q_∞= 20 psf and q_∞= 30 psf, respectively.

C_L and C_D calculations are based on the pressure readings and the angle of attack, and both have their own sources of error. Pressure readings are given from the ESP pressure scanners which were chosen, in part, for their accuracy. Once calibrated, the pressure scanners have a rated ±0.05% accuracy. AoA is controlled by the motor. Once programmed using the Kollmorgen Workbench software, the motor has a rated accuracy up to an arc-second, which enables AoA to be set very consistently. However, once the wind tunnel is turned on, the torque generated from the system shifts AoA and effectively negates the accuracy of the motor. During testing, the ASM angle reader is used to monitor this shift and at certain points approximately a 0.5º shift in AoA was registered. For this reason, when calculating lift and drag, AoA was rounded to the nearest integer. AoA uncertainty is estimated to be ±0.5º. Taking into account these two factors, an uncertainty range for C_L and C_D can be estimated. The lift and drag results for the unequal blowing case with estimated uncertainty are shown in Figures 47 and 48, respectively. Based on these results the uncertainty for both lift and drag is estimate to be C_L±.03 and C_D±.03, shown as follows with error bars.

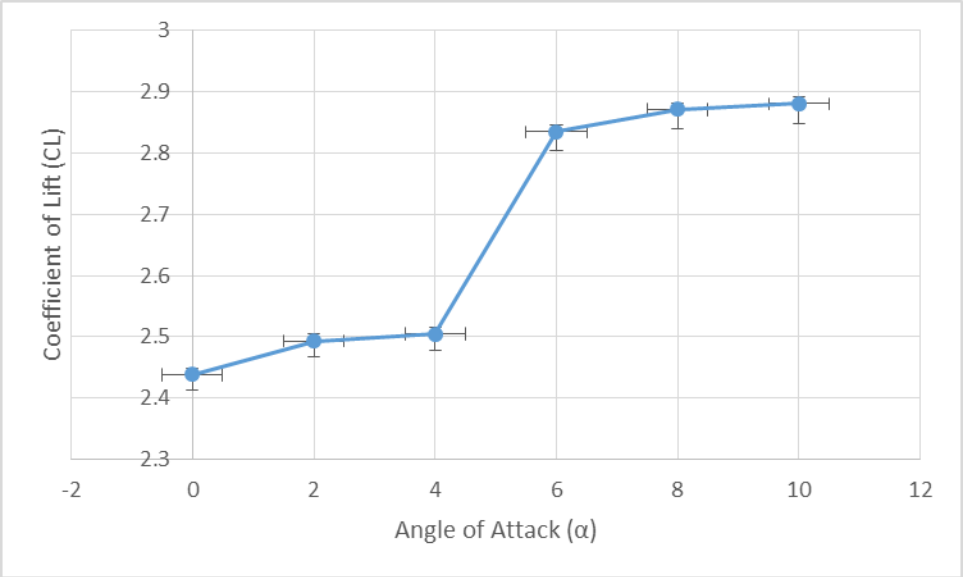

Figure 47. Unequal Blowing lift results with uncertainty estimates

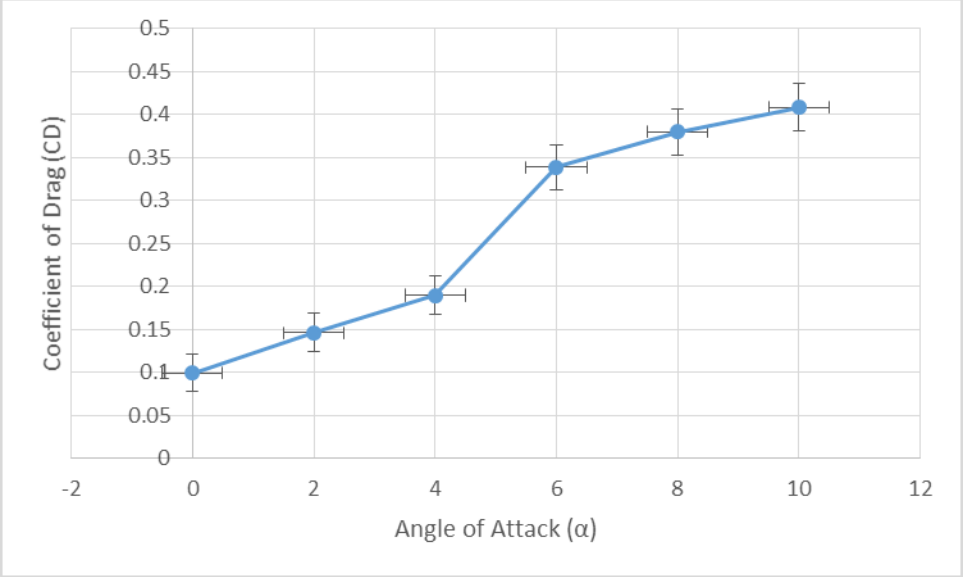

Figure 48. Unequal blowing drag results with uncertainty estimate

CHAPTER 5. SUMMARY AND DISCUSSION

Conclusions

The effectiveness of steady blowing AFC to increase lift over a laminar high-lift configuration airfoil was investigated experimentally. The study focused on four steady blowing AFC cases from different slot locations and varying C_μ. Each of the four cases was able to increase lift; the unequal blowing case was able to achieve the highest gain in lift, 31% and 43% over the baseline for q_∞ = 30psf and 20 psf, respectively. These results are encouraging, but are under anticipated values. In comparison, both the studies by Burnazzi (2013) and Bright (2012) achieved approximately 100% increase in lift. After investigating the pressure distributions from each case, it is evident that the test were very successful in generating high-lift around the leading edge, but separation occurs over the deflected flap. This separation leads to higher pressure and lower speeds around the shoulder over the deflected flap, effectively negating the Coanda effect. The Coanda effect, which enables the BL to accelerate and stay attached over a curved surface, is the demonstrated by low pressure peaks at the shoulder of the deflected flap. Without a proper Coanda effect over the deflected flap, low pressure peaks are not seen in this study. In both the studies by Burnazzi (2013) and Bright (2012), low pressure peaks between $-10 \leq C_p \leq -20$ were seen around the leading edge and shoulder of the deflected flap and are essential to increased lift. The cause of this separation has been attributed to a few different factors: tunnel blockage, non-uniform jet velocity, model imperfections (i.e. steps and gaps), and the use of two different materials. Tunnel blockage is considered the largest problem.

Tunnel Blockage can greatly affect test results. As AoA increases, the frontal area of the airfoil continues to increase and near-wall effects can begin to contribute to data error. The airfoil spans the entire vertical cross section of the wind tunnel, and by 10 degrees tunnel blockage approaches 12%. Tunnel blockage effects are normally considered to be minor when blockage is less than 10%, but since this is a high-lift study the effected flow is much larger than normal. Therefore, the effective tunnel blockage can be much larger than the calculated tunnel blockage. Blockage has a greater effect on drag, so this could be cause of the leveling off in the drag curves. As angle is increased, tunnel blockage becomes greater, and the lift-induced drag cannot continue to increase. Using particle velocity imaging (PIV) and testing the model in a much larger wind tunnel would be needed to fully determine the flow effects and correct this problem.

Non-uniform jet exit velocity is another possible problem. If the jet exit velocity is not uniform, the effects of momentum addition could vary along the span of the airfoil. Before testing began, the uniformity of each slot was measured outside of the wind tunnel at constant back pressure and was consistent along the span, but was not tested again once installed in the wind tunnel. The pressure of each plenum was monitored closely during test to avoid uniformity problems. Since all cases were tested multiple times for both q_∞ =30psf and q_∞ =20psf, each with similar results, it is unlikely jet uniformity was the problem.

Another possible cause for the underperforming results is that during testing small steps and gaps were discovered along the airfoil assembly. A step was seen between the aft plenum assembly and the aluminum tail components, directly before the shoulder of the deflected flap (Appendix B). This step could cause a minor pressure build up before the shoulder at low AOA. As AoA increases the effects of this step become greater, and more

pressure begins to build up. Once pressure has significantly built up, the Coanda effect is disrupted and eventually leads to separation. Each pressure distribution shows a higher pressure at 81% chord, directly before the step. Although the evidence supporting this theory is compelling, the size of the steps and gaps are very small and it is unlikely they could have such a profound effect on the results. To further determine if these discontinuities are effecting the data and correct for this, the model has to be reassembled and these discontinuities must be removed. Time constraints made this impractical for this study.

APPENDIX A. MATLAB CODE

```
%% Patrick Clayton Lift_Calc.m
clc
close all
clear all
format compact

%% Input Cp data
prompt = 'Cp file name?:';
cpfile = input(prompt,'s');
% cpfile = 'A2_sweep.txt';
cp = load(cpfile);

[m,n] = size(cp);
k=m-1;

load PP_position.txt  %load pressure port locations
x = PP_position(:,1);
y = PP_position(:,2);

%% area calculations
for i = 1:size(x)-1
    dx(i)=x(i+1)-x(i);
    dy(i)=y(i+1)-y(i);
    x_bar(i) = .5*(x(i)+x(i+1));
    y_bar(i) = .5*(y(i)+y(i+1));
end

for j = 1:n
    for i = 2:k
        cp_bar(i,j) = .5*(cp(i,j)+cp(i+1,j));
    end
end

%% force components
for j =1:n
    for i = 1:size(x)-1
        dA1(i,j) = -cp_bar(i,j)*dy(i);
        dN1(i,j) = cp_bar(i,j)*dx(i);
        dMLE(i,j) = -dN1(i,j)*x_bar(i)+dA1(i,j)*y_bar(i);
    end
end



q=30;
c=18/12;
cA = sum(dA1);
cN = sum(dN1);
C_MLE = sum(dMLE);
```

```
%% lift, drag and moment calculation
for j=1:n
    AoA(j) = cp(1,j); %takes AoA from first line of input file
    % AoA written on first line of each of the calculated parameters
    cL(1,j)=AoA(j);
    cD(1,j)=AoA(j);
    x_cp(1,j) = AoA(j);
    C_MC4(1,j) = AoA(j);
    C_MC2(1,j) = AoA(j);


    x_cp(2,j) = -C_MLE(j)/cN(j);
    C_MC4(2,j) = C_MLE(j)+.25*cN(j);
    C_MC2(2,j) = C_MLE(j)+.5*cN(j);

    cL(2,j) = cN(j)*cosd(AoA(j))-cA(j)*sind(AoA(j));
    cD(2,j)= cN(j)*sind(AoA(j))+cA(j)*cosd(AoA(j));
end
```

APPENDIX B. ADDITIONAL TEST DESIGN FIGURE

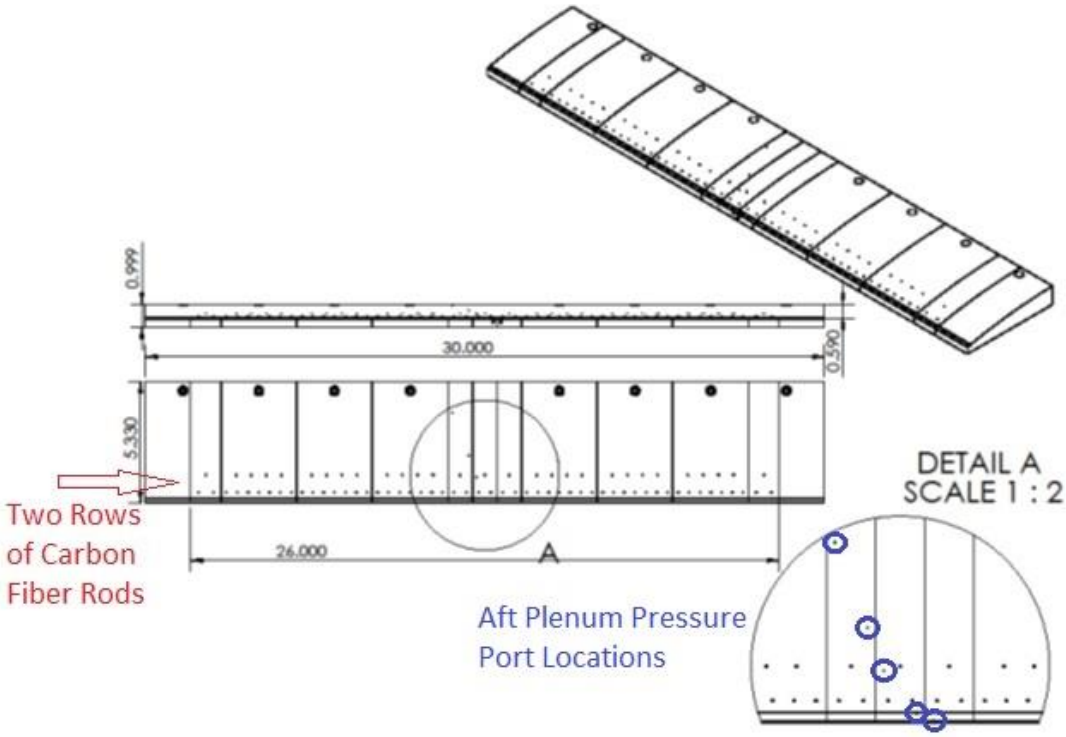

Aft plenum assembly with pressure port detail

REFERENCES

Abbas, A., de Vicente, J., & Valero, E. (2012). Aerodynamic technologies to improve aircraft performance. *Aerospace Science and Technology, 28*(1), 100-132.

Anderson, Jr., J. D. (2011). *Fundamentals of aerodynamics.* London, U.K.: McGraw-Hill.

Bright, M. M., Korntheuer, A., Komadina, S., & Lin, J. C. (2012). *Development of advanced high lift leading edge technology for laminar flow wings*. Paper presented at the *51st AIAA Aerospace Sciences Meeting including the New Horizons Forum and Aerospace Exposition*, American Institute of Aeronautics and Astronautics, Grapevine, TX.

Burnazzi, M., & Radespiel, R. (2013). Design of a Droopnose Configuration for a Coanda Active Flap Application. Paper presented at the *51st AIAA Aerospace Sciences Meeting including the New Horizons Forum and Aerospace Exposition*, American Institute of Aeronautics and Astronautics, Grapevine, TX.

Collis, S. S., Joslin, R. D., Seifert, A., & Theofilis, V. (2004). Issues in active flow control: theory, control, simulation, and experiment. *Progress in Aerospace Sciences, 40*(4-5), 237-289.

Dunne, R. (2010). *Wind Tunnel Simulation of Flow Control with Pulsed Impinging Air Jets.* Medford, MA: Tufts University.

Gad-El-Hak, M., & Bushnell, D. (1991). Separation control: Review. *ASME, Transactions, Journal of Fluids Engineering, 113*, 5-30.

Greenblatt, D., & Wygnanski, I. J. (2000). The control of flow separation by periodic excitation. *Progress in Aerospace Sciences, 36*(7), 487-545.

Greenblatt, D., Neuburger, D., & Wygnanski, I. (2001). Dynamic stall control by intermittent periodic excitation. *Journal of Aircraft, 38*(1), 188-190.

Jabbal, M., Liddle, S. C., & Crowther, W. J. (2010). Active flow control systems: Architectures for civil transport aircraft. *Journal of Aircraft, 47*(6), 1966-1981.

Joslin, R. D. (1998). *Overview of laminar flow control*. Hampton, VA: National Aeronautics and Space Administration, Langley Research Center. Distributed by National Technical Information Service, Springfield, VA.

Joslin, R. D., & Miller, D. N. (2009). *Fundamentals and applications of modern flow control*. Reston, VA: American Institute of Aeronautics and Astronautics.

Nichino, T., Hahn, S., & Shariff, K. (2010). *LES of high-Reynolds-number Coanda flow separating from a rounded trailing edge of a circulation control airfoil.* Paper presented at the 8th International ERCOFTAC Symposium on Engineering Turbulence Modelling and Measurements (ETMM8), European Research Community of Flow, Turbulence and Combustion, Marseille, France.

Patterson, C. (2011). *Evaluation of pulsed & steady blowing flow control in a slotted leading edge configuration.* Medford, MA: Tufts University.

Pfingsten, K. C., Radespiel, R., & Kamruzzaman, M. (2005). *Use of upper surface blowing and circulation control for gapless high-lift configuration.* Paper presented at the CEAS/KATnet Conference on Key Aerodynamic Technologies, Bremen, Germany.

Schatz, M., Thiele, F., Petz, R., & Nitsche, W. (2004). *Separation control by periodic excitation and its application to a high-lift configuration.* Paper presented at the 2nd AIAA Flow Control Conference, American Institute of Aeronautics and Astronautics Portland, OR.

Seifert, A., Darabi, A., & Wyganski, I. (1996). Delay of airfoil stall by periodic excitation. *Journal of Aircraft, 33*(4), 691-698.